















Release of linker histone from the nucleosome driven by polyelectrolyte competition with a disordered protein

Pétur O. Heidarsson^{1,5,9}  , Davide Mercadante^{1,6,9} , Andrea Sottini¹ , Daniel Nettels¹,
Madeleine B. Borgia^{1,7} , Alessandro Borgia^{1,7} , Sinan Kilic^{2,8} , Beat Fierz² , Robert B. Best³  
and Benjamin Schuler^{1,4}  

Highly charged intrinsically disordered proteins are essential regulators of chromatin structure and transcriptional activity. Here we identify a surprising mechanism of molecular competition that relies on the pronounced dynamical disorder present in these polyelectrolytes and their complexes. The highly positively charged human linker histone H1.0 (H1) binds to nucleosomes with ultrahigh affinity, implying residence times incompatible with efficient biological regulation. However, we show that the disordered regions of H1 retain their large-amplitude dynamics when bound to the nucleosome, which enables the highly negatively charged and disordered histone chaperone prothymosin α to efficiently invade the H1-nucleosome complex and displace H1 via a competitive substitution mechanism, vastly accelerating H1 dissociation. By integrating experiments and simulations, we establish a molecular model that rationalizes the remarkable kinetics of this process structurally and dynamically. Given the abundance of polyelectrolyte sequences in the nuclear proteome, this mechanism is likely to be widespread in cellular regulation.

A large fraction of the human genome codes for proteins that contain extensive disordered regions or even lack any well-defined three-dimensional structure¹. These intrinsically disordered proteins (IDPs) are known to play important roles in the cell nucleus, especially in the formation of nuclear organelles via liquid–liquid phase separation, chromatin condensation and transcriptional regulation, via mediating key interactions with other proteins or nucleic acids^{2,3}. DNA- and RNA-binding proteins often contain disordered regions highly enriched in positively charged residues^{4,5}, which are expected to facilitate electrostatic interactions with their cellular targets⁵. The affinities can be remarkably high, even if no structure is formed upon binding^{6,7}. Such polyelectrolyte interactions have long been known in the fields of polymer chemistry and soft matter physics^{8,9}, but their importance in biology only recently started to be recognized^{6,7,10–12} and is thus largely unexplored.

A ubiquitous group of nuclear proteins with disordered polycationic regions are the histones, which are responsible for packaging DNA into chromatin, predominantly via their strong electrostatic interactions with the polyanionic nucleic acids¹³. Among these, the linker histones are particularly notable¹⁴: they are largely disordered and highly positively charged, with two disordered regions flanking a small folded globular domain. By binding to the linker DNA on the nucleosome (Fig. 1a), linker histones contribute to chromatin condensation and transcriptional regulation^{14–17}. The extent of disorder in the complex between the nucleosome and linker histones suggests that it may have important roles for function¹⁶. For

example, it was recently demonstrated that the linker histone H1 can promote the formation of liquid–liquid phase separation of reconstituted chromatin arrays under physiological conditions¹⁸.

Here, we show how the disordered tail regions of H1 facilitate a remarkable mechanism of molecular chaperoning that keeps the H1–nucleosome complex in a rapid association–dissociation equilibrium despite the extremely high affinity of the interaction. By integrating single-molecule experiments and simulations, we establish a molecular model of the H1–nucleosome complex, in which the H1 tails remain highly disordered and dynamic even when bound. We demonstrate that the highly negatively charged and disordered human protein prothymosin α (ProT α), a well-known histone chaperone^{19–22} that forms a high-affinity disordered complex with linker histone H1 (ref. 6), can efficiently displace H1 from the nucleosome and accelerate its dissociation. The results can be explained by a mechanism in which ProT α initially invades the linker-histone/nucleosome complex and forms interactions with H1 mediated by the extensive disorder in both proteins, resulting in facilitated H1 dissociation. The underlying process of competitive substitution²³ via a transient ternary complex may be widespread in IDP-mediated nuclear interactions.

Results

Probing H1–nucleosome interactions. To understand the interactions between nucleosomes, H1 and ProT α , we probed both the conformational distributions of these highly disordered molecules as well as the equilibria and kinetics of their complex formation and

¹Department of Biochemistry, University of Zurich, Zurich, Switzerland. ²Institut des Sciences et Ingénierie Chimiques (ISIC), Ecole Polytechnique Fédérale de Lausanne (EPFL), Lausanne, Switzerland. ³Laboratory of Chemical Physics, National Institute of Diabetes and Digestive and Kidney Diseases, National Institutes of Health, Bethesda, MD, USA. ⁴Department of Physics, University of Zurich, Zurich, Switzerland. ⁵Present address: Department of Biochemistry, Science Institute, University of Iceland, Reykjavík, Iceland. ⁶Present address: School of Chemical Sciences, University of Auckland, Auckland, New Zealand. ⁷Present address: Department of Structural Biology, St. Jude Children's Research Hospital, Memphis, TN, USA. ⁸Present address: Novo Nordisk Foundation Center for Protein Research, University of Copenhagen, Copenhagen, Denmark. ⁹These authors contributed equally: Pétur O. Heidarsson, Davide Mercadante.  e-mail: pheidarsson@hi.is; robert.best2@nih.gov; schuler@bioc.uzh.ch

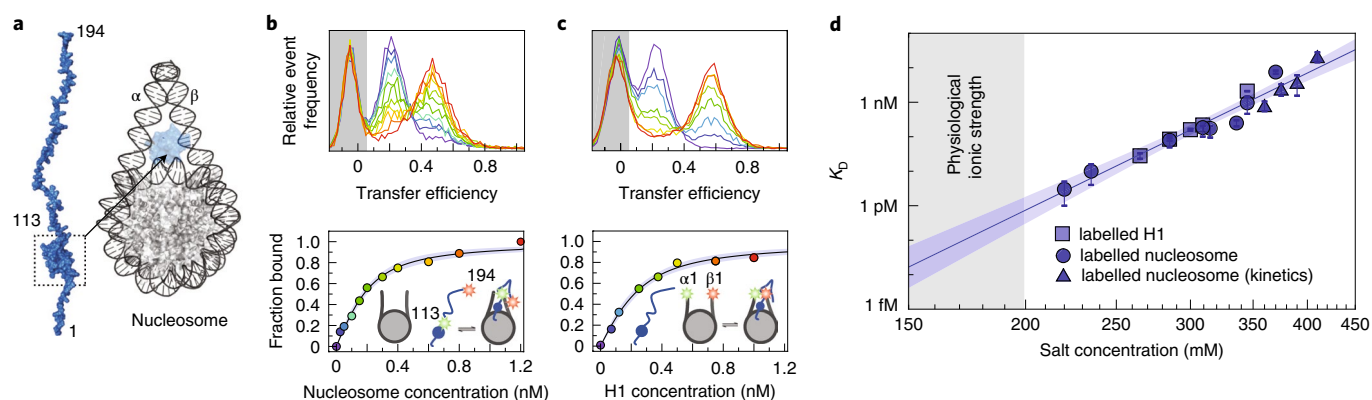


Fig. 1 | H1 binds nucleosomes tightly but reversibly. **a**, Structural representation of histone H1 and the nucleosome–H1 complex, with the position of the H1 globular domain on the nucleosome indicated (PDB no. 5NLO)²⁹. H1, blue; DNA, dark grey; core histones, light grey. The entry and exit linker DNA are denoted α and β , respectively. **b,c**, Binding of H1 to the nucleosome. Single-molecule transfer efficiency histograms and binding isotherms (see symbols in binding isotherms below for the colour code of concentrations) of freely diffusing H1 fluorescently labelled at positions 113 and 194 (**b**) or nucleosomes labelled at positions $\alpha 1$ and $\beta 1$ (**c**) titrated with the corresponding unlabelled binding partner (10 mM tris(hydroxymethyl)aminomethane (Tris), 0.1 mM ethylenediaminetetraacetic acid (EDTA), pH 7.4, 300 mM KCl). See cartoon insets for illustration of labelling positions. Transfer efficiency range dominated by signal from molecules lacking an active acceptor dye shaded in grey. **d**, Equilibrium dissociation constant (K_D) as a function of salt concentration, from binding isotherms using labelled H1 (squares) or labelled nucleosomes (circles), and from rate coefficients ($K_D = k_{off}/k_{on}$) measured with surface-immobilized labelled nucleosomes (triangles). The data were fit and extrapolated to the physiological ionic-strength range (grey-shaded area) with the Lohman–Record model²⁴ (solid line with shaded 95% confidence band). Error bars indicate uncertainties estimated from dilution errors (see Methods for details).

dissociation. We first investigated the binding of the human linker histone H1.0 (referred to herein as H1) to nucleosomes with confocal single-molecule spectroscopy combined with Förster resonance energy transfer (FRET). We attached a donor and an acceptor fluorophore at positions 113 and 194 in H1, spanning its disordered C-terminal region (Fig. 1a), and monitored the binding to nucleosomes freely diffusing in solution.

Unbound H1 shows a low mean FRET efficiency, $\langle E \rangle$, as expected for a highly expanded configuration due to intramolecular repulsion between the positive charges in H1 (refs. 6,24,25). Upon addition of unlabelled reconstituted nucleosomes based on the 197-base-pair (bp) 601 Widom sequence²⁶ (Fig. 1a), a population with higher $\langle E \rangle$ is formed (Fig. 1b), indicating a compaction of H1 on binding, in line with previous results²⁷. From the bound fraction as a function of nucleosome concentration, we obtained the equilibrium dissociation constant (K_D), which is highly dependent on salt concentration: across the range where reliable measurements were feasible (220–410 mM), K_D increases from ~ 3 pM to ~ 10 nM (Fig. 1d and Supplementary Table 1). Measurements at lower salt concentrations are complicated by the high and non-specific affinity of H1 to surfaces⁶, but extrapolation suggests subpicomolar K_D values in the physiological ionic-strength range below 200 mM—even slightly tighter than estimated previously²⁸. To control for the possible influence of dye labelling on the interaction, we also performed single-molecule measurements with the fluorophores attached to the termini of the nucleosomal linker DNA arms (positions $\alpha 1$ and $\beta 1$; Fig. 1a) and titrated with unlabelled H1 (Fig. 1c). The $\langle E \rangle$ value increases upon binding, in line with the expected closure of the linker DNA arms in the H1-bound nucleosome^{29–31}. The resulting K_D values agree with the measurements using labelled H1 over a wide range of salt concentrations (Fig. 1d), attesting to the robustness of the approach and to a lack of strong perturbations by the dyes.

The pronounced salt concentration dependence of K_D (Fig. 1d) reflects the important role of electrostatic interactions in the binding process. Although a substantial fraction of the DNA charge in the nucleosome is compensated by the histone octamer, the resulting polyanion–polycation complex retains a large negative net charge, especially at the dyad and on the linker DNA, which favours the

binding of additional positively charged proteins such as H1 (ref. 13). The interaction of H1 with the nucleosome can be described in terms of a counterion exchange reaction, in which H1 binding results in a release of inorganic counterions—under our experimental conditions mainly chloride ions associated with H1 and potassium ions associated with the DNA^{32,33}. The entropy gain from this counterion release is a major thermodynamic driving force for such protein–DNA interactions, and the dependence of the corresponding K_D on salt concentration has been shown for a variety of systems to be well approximated by the relation

$$\log K_D = \log [K_D(1 \text{ M})] - \Delta n \log c_M,$$

where c_M is the salt concentration, Δn is the number of released counterions, and the K_D at 1 M salt reports on non-electrostatic contributions to binding³². Applied to the H1–nucleosome interaction (Fig. 1d), we obtain a release of $\Delta n = 13 \pm 1$ inorganic ions, and the K_D extrapolated to 1 M salt is ≥ 1 mM, indicating a weak non-electrostatic contribution to binding, possibly mediated by the interactions of the H1 globular domain with the DNA at the dyad^{29,34}.

Association kinetics of H1 on immobilized nucleosomes. For probing the kinetic mechanism of H1–nucleosome interactions, we immobilized labelled nucleosomes via a biotin–streptavidin tether on polyethylene-glycol-passivated cover slides and recorded fluorescence time traces from single nucleosomes with confocal single-photon counting for up to several minutes (Fig. 2a, Supplementary Fig. 1). Nucleosomal unwrapping events were identified by persistent changes in transfer efficiency^{35,36} and excluded from the analysis (Supplementary Fig. 1c). In the presence of low concentrations of unlabelled H1, the time traces exhibit the characteristic anti-correlated changes in donor and acceptor fluorescence expected from the association and dissociation of individual H1 molecules, with high $\langle E \rangle$ in the bound state and low $\langle E \rangle$ in the unbound state (Fig. 2a). To quantify the kinetics, thousands of such H1 association and dissociation events were analysed by likelihood maximization based on a two-state Markov model³⁷ (Fig. 2, see Methods for details), which describes the data well (Fig. 2a).

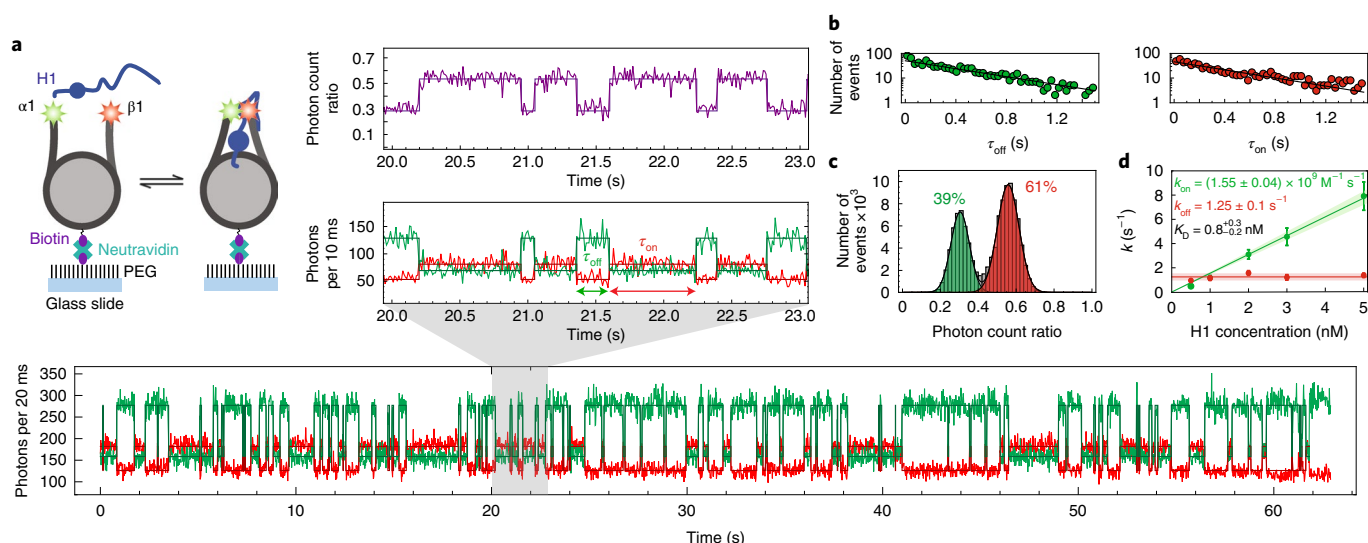


Fig. 2 | H1 binds nucleosomes with diffusion-limited association rates. a, Example of a single-molecule fluorescence time trace of 2 nM unlabelled H1 binding to surface-immobilized labelled nucleosomes (see cartoon; PEG, polyethylene glycol) at 360 mM salt (acceptor signal, N_A , red; donor signal, N_D , green). An expanded segment is shown above, along with the photon count ratio ($N_A/(N_A + N_D)$, purple) and appropriately scaled state trajectories (dark green, red, purple) based on Viterbi analysis with a two-state model. **b**, Dwell-time distributions for the unbound (green) and bound (red) states with exponential fits (solid lines). **c**, Photon count ratio histograms from 46 fluorescence time traces at 360 mM salt and 2 nM H1, showing the unbound (green) and bound (red) populations. **d**, Observed association rate (green) and dissociation rate coefficient (red) as a function of H1 concentration at 360 mM salt concentration and fits assuming a one-to-one binding model (solid lines) with resulting values. Error bars show one standard deviation estimated from ten bootstrapping trials; shaded bands for all fits represent 95% confidence intervals.

The resulting association (k_{on}) and dissociation (k_{off}) rate coefficients yielded values of K_D in accord with the free-diffusion experiments (Fig. 1d and Supplementary Table 1), indicating that surface immobilization does not interfere with H1 binding. Association is extremely rapid, with rate coefficients at the diffusion limit, $>10^9 \text{ M}^{-1} \text{ s}^{-1}$ (Supplementary Table 1), which indicates binding without a substantial activation barrier. The increase in affinity with decreasing salt concentration (Fig. 1d) is dominated by a decrease in k_{off} , whereas k_{on} is much less salt dependent (Supplementary Fig. 2 and Supplementary Table 1). The similarity of the salt concentration dependences of k_{off} (12 ± 1 ions bound upon dissociation; Supplementary Fig. 3a) and K_D (13 ± 1 ions bound upon dissociation; Fig. 1d) further supports a binding mechanism that is downhill in free energy.

These results illustrate a classic conundrum regarding H1–nucleosome interactions^{28,38,39}: at physiological ionic strengths, dissociation of H1 from the nucleosome *in vitro* is much too slow to be compatible with efficient cellular regulation of transcription and chromatin condensation⁴⁰. At 165 mM salt, for instance, extrapolating our results yields an average dwell time in the bound state of 3_{-1}^{+2} hours (Supplementary Fig. 3a), similar to previous results *in vitro*⁴¹ but much longer than the timescale of about a minute observed in cells^{38,39}. Clearly, other cellular factors must be involved in regulating the interaction of H1 with chromatin.

ProTα efficiently displaces H1 from the nucleosome. A well-known linker histone chaperone is ProTα^{19–22}, which binds to H1 with high affinity^{6,12,42,43} and is thus expected to compete with the nucleosome for H1 binding. Indeed, if the experiments probing H1–nucleosome binding are performed in the presence of ProTα, the kinetics of the system change markedly (Fig. 3a). For example, at 340 mM salt and 3 nM H1 in the absence of ProTα, H1 remains nucleosome-bound for ~ 4 s on average, and association occurs rapidly after dissociation, leading to an unbound population of only $\sim 2\%$, just enough to detect occasional dissociation events in fluorescence time traces. At lower salt concentrations, the H1–nucleosome

affinity is too high to detect spontaneous dissociation. Upon addition of ProTα, the frequency of transitions to low $\langle E \rangle$ increases (Fig. 3a), with a change in rate from 0.3 s^{-1} to 8 s^{-1} when the ProTα concentration is increased from 0 to 140 μM (Fig. 3b). This rate enhancement occurs for a wide range of salt concentrations, and it exceeds two orders of magnitude at near-physiological salt concentrations (Supplementary Fig. 3a). Intra- and intermolecular single-molecule FRET experiments on freely diffusing molecules confirm the accelerated and complete dissociation of H1 from the nucleosome by ProTα (Fig. 3c–f and Supplementary Fig. 3). Thermodynamically, this reaction can be described as a competition between two polyanions, ProTα and DNA, for the polycation H1; the larger number of counterions released upon binding of H1 to ProTα (18 ± 1)^{6,43} compared to the nucleosome (13 ± 1 ; Fig. 1d) contribute entropically to the release of H1. Notably, the tens-of-micromolar ProTα concentrations we require for enhanced H1 dissociation are in the range reported for intracellular ProTα⁴⁴, which is thus likely to contribute to the high mobility of H1 in cells^{38,39}. What is the mechanism underlying this rate enhancement by ProTα?

The observed increase in rate (Fig. 3b) is not compatible with the simplest competition mechanism, where H1 forms exclusively binary complexes, either with the nucleosome or with ProTα. In this case, H1 would first have to dissociate from the nucleosome before binding to ProTα. In other words, dissociation of H1 from the nucleosome would be a unimolecular reaction with a rate independent of ProTα concentration (red dashed line in Fig. 3b), in contrast to what we observe. Moreover, the observed rate of transitions to high $\langle E \rangle$ changes much less than expected for the association rate in this mechanism, where the presence of ProTα should sequester free H1 to an extent that H1 association would decrease to a virtually undetectable level (green dashed line in Fig. 3b). These deviations from the simplest competition mechanism are a typical indication for the formation of ternary complexes, a paradigm that has recently emerged for gene regulation and usually involves multivalent interactions^{45–49}. Such ternary complex formation immediately suggests itself for complexes of IDPs such as H1 and ProTα, whose interactions can

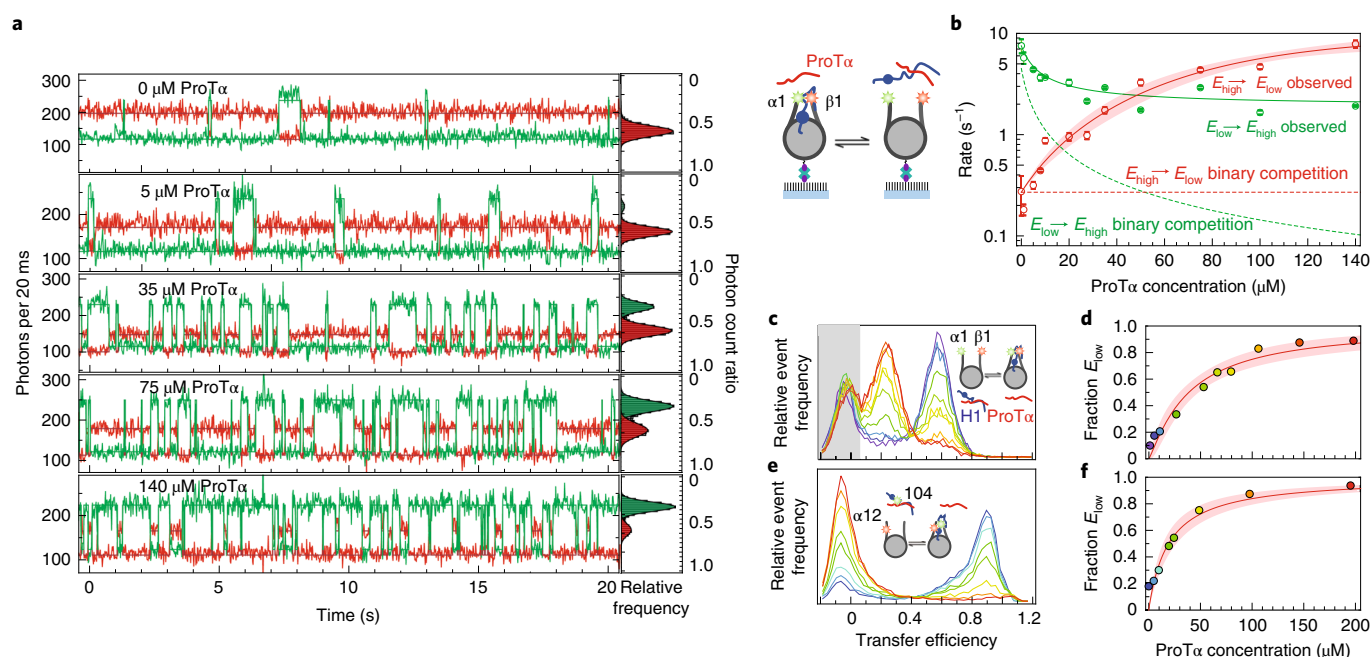


Fig. 3 | ProT α facilitates H1 dissociation from the nucleosome. **a**, Fluorescence time traces monitoring H1 binding to surface-immobilized nucleosomes (cartoon) at different ProT α concentrations and corresponding photon count ratio histograms (see Fig. 2 for details). **b**, Kinetic analysis of time traces, with observed transition rates from low to high FRET efficiency ($E_{\text{low}} \rightarrow E_{\text{high}}$, green symbols) and from high to low FRET efficiency ($E_{\text{high}} \rightarrow E_{\text{low}}$, red symbols) as a function of ProT α concentration, described with different kinetic models (dashed line, competition with binary interactions only; solid line, competition including ternary-complex formation; see Methods for details). Error bars show one standard deviation estimated from ten bootstrapping trials. **c–f**, Transfer efficiency histograms (**c** and **e**) from free-diffusion single-molecule FRET experiments in the presence of different ProT α concentrations (see symbols in binding isotherms for the colour code, and cartoon insets for illustration of components and labelling positions) and corresponding fractional populations (**d** and **f**). Intramolecular FRET of double-labelled nucleosomes in the presence of 1 nM unlabelled H1, at increasing concentration of unlabelled ProT α (shown in the cartoon inset; **c**) and the corresponding fraction of low-FRET population (symbols in **d**) fit with a binding isotherm (**d**). Intermolecular FRET between 5 nM acceptor-labelled nucleosomes and 100 pM donor-labelled H1, with increasing concentration of unlabelled ProT α (shown in the cartoon inset; **e**) and the corresponding fraction of low-FRET population (symbols in **f**) fit with a binding isotherm (**f**). Note that in **c**, the peak at FRET efficiency $E \approx 0$ (grey shading) originates from molecules lacking an active acceptor fluorophore, resulting in an amplitude independent of ProT α concentration; in **e**, we explicitly use the increase in the peak at $E \approx 0$ and concomitant decrease of the peak at $E \approx 0.9$ to monitor donor-labelled H1 dissociation. Data in all panels were collected at 340 mM salt; shaded bands for fits represent 95% confidence intervals.

be considered an extreme case of multivalency^{10,45,49}: if the positively charged tails of H1 remain largely disordered and dynamic while bound to the nucleosome, as suggested by recent experimental work on the C-terminal region of H1 bound to double-stranded DNA⁷ and by simulations^{30,50}, the negatively charged ProT α would still be able to invade the complex via local association–dissociation events and bind to H1 while both proteins remain disordered⁶. To obtain more insight into the underlying molecular mechanism of ProT α action, we thus first sought a structural description of H1 on the nucleosome.

H1 is highly disordered and dynamic on the nucleosome. The globular domain of H1 is known to localize to the dyad axis and interact with the nucleosomal core DNA and both linkers^{29,31}. However, the conformational distributions of the disordered regions of H1 on the nucleosome have been difficult to elucidate because of their dynamics and lack of persistent structure^{4,7,29,51}. Since fluctuations in distance cause fluctuations in the fluorescence intensity of donor and acceptor⁵², we can monitor molecular motion in single-molecule FRET experiments with nanosecond fluorescence correlation spectroscopy (nsFCS⁵³; Fig. 4a and Supplementary Fig. 4). Indeed, H1 shows pronounced long-range chain dynamics (Fig. 4a) on the 100-ns timescale characteristic of disordered proteins⁵², both in isolation⁶, bound to the nucleosome (Fig. 4a), and bound to 25-bp double-stranded DNA, in agreement with recent NMR results⁷ and with the insensitivity of the intermolecular FRET efficiency between H1 and 25-bp double-stranded DNA to

label position (Supplementary Fig. 5a,b). Distance fluctuations on this timescale can be observed throughout the C-terminal region of H1, as well as between the ends of the nucleosomal linker DNA (Supplementary Fig. 4b,c), highlighting the exceedingly dynamic nature of the complex. The presence of broad distance distributions and rapid molecular motion resulting from disorder is further supported by fluorescence lifetime analysis (Supplementary Fig. 6). These results suggest a picture in which local segments of the H1 tails continuously disengage and reengage in non-specific electrostatic interactions with the DNA, leading to rapid local and global reconfiguration dynamics.

We thus require a molecular model that takes this dynamical disorder into account, allows a description of H1 in terms of a structurally diverse conformational ensemble and can be optimized based on experimental data. In view of the large system size, we employed a coarse-grained simulation model that captures both the known structure of the nucleosome and the pronounced dynamics of the linker DNA and the disordered regions of H1. We used a ‘top-down’ coarse-grained model based on matching experimental observations, rather than a ‘bottom-up’ coarse-grained model matched to all-atom simulations³⁰. We combined a structure-based model^{54,55} for the nucleosomal core particle and the globular domain of H1 and its position on the dyad based on the crystal structure (Protein Data Bank (PDB) no. 5NL0)²⁹ with a polymer-like representation of the histone tails. The interaction between disordered regions of histones and DNA was encoded in terms of non-specific

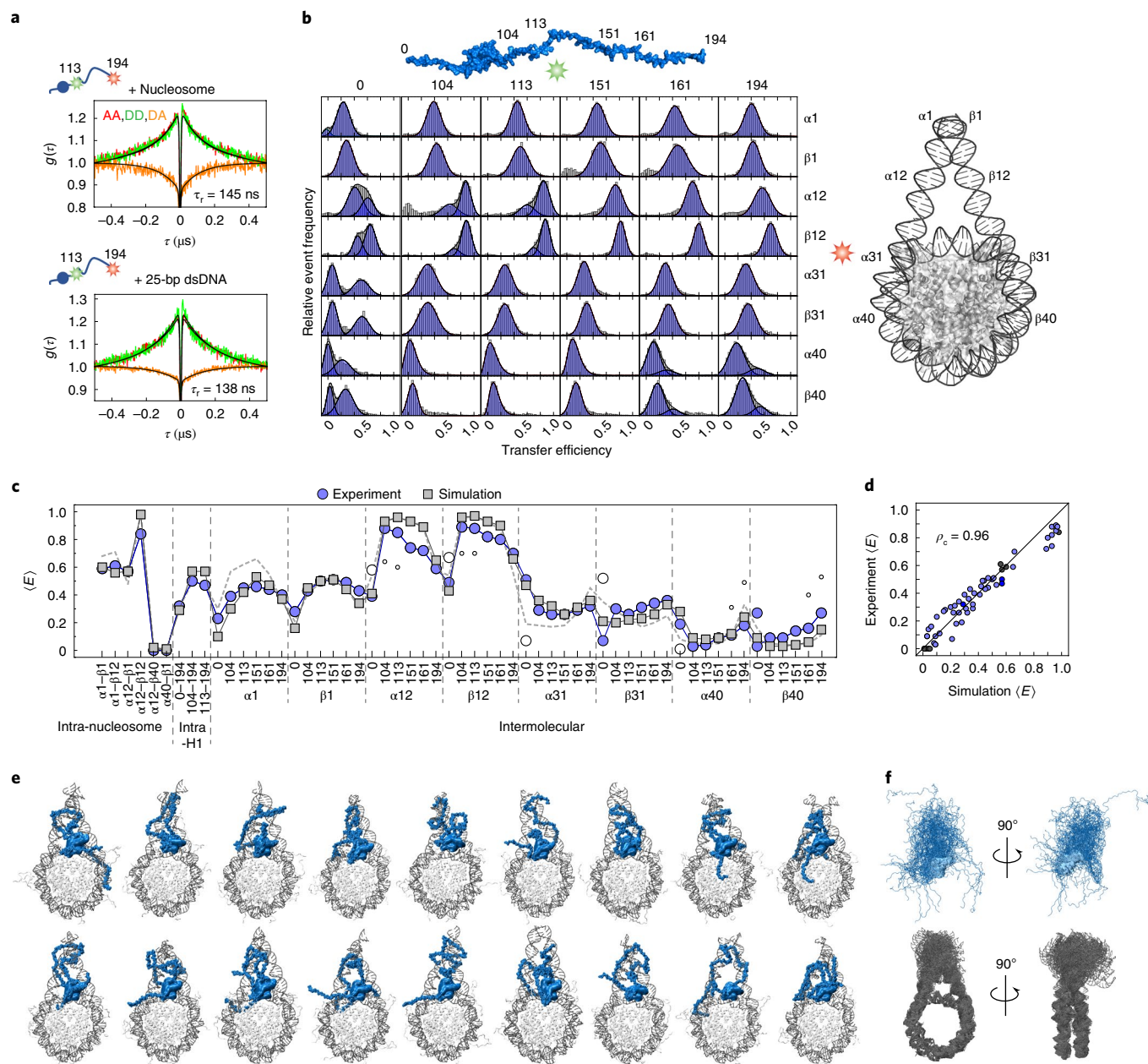


Fig. 4 | H1 remains disordered and dynamic on the nucleosome. a, nsFCS of double-labelled H1 bound to the nucleosome (top) and double-stranded 25-bp DNA (bottom), with donor-donor (DD, green), acceptor-acceptor (AA, red) and donor-acceptor (DA, orange) correlations, $g(\tau)$, with fits (see Methods for details; τ_r , chain reconfiguration times; τ , lag time). **b**, Intermolecular single-molecule FRET experiments with dyes at different positions along the H1 (donor dye, green star) and nucleosome sequences (acceptor dye, red star). Labelling positions are indicated as numbers along the structural representations. Subpopulations are fit with Gaussian peak functions (black lines). **c**, Comparison between average FRET efficiencies, $\langle E \rangle$, from experimental subpopulations and simulation for 57 different labelling pairs (**b** and Supplementary Fig. 5). Filled blue circles, main experimental FRET population; empty circles, minor experimental FRET population (size of symbol indicates population size); grey squares, $\langle E \rangle$ from simulations using the H1 globular domain orientation as in structure 5NLO (ref. ²⁹); dashed line, $\langle E \rangle$ from simulations using the crystal structure but with the H1 globular domain rotated by 180° on the dyad. **d**, Correlation between experimental and simulated $\langle E \rangle$, with concordance correlation coefficient, ρ_c . **e**, Representative snapshots of the H1-nucleosome complex from simulations (see Methods for details, and Supplementary Video 1). **f**, Overlay of 50 conformations of H1 (top) and nucleosome (bottom) in the complex. All measurements and simulations performed at 165 mM salt concentration.

short-range and electrostatic interactions⁵⁶, including a screening term to account for the experimental ionic strength (see Methods for details). To attain a realistic description of the disordered and dynamic parts of the H1-nucleosome complex, we adjusted the strength of the short-range protein-DNA interactions via a single parameter to maximize the agreement between the measured FRET efficiencies and those computed from the simulation ensemble.

Although this model does not explicitly represent counterions and all details of chemical structure⁵⁷, its previous success in explaining the interaction of H1 with ProTα in terms of both overall structure and affinity⁶ indicates that it can be used to obtain insight into the overall properties of the system.

To test and optimize the model of H1 on the nucleosome, we obtained FRET data reporting on a total of 57 intra- and inter-

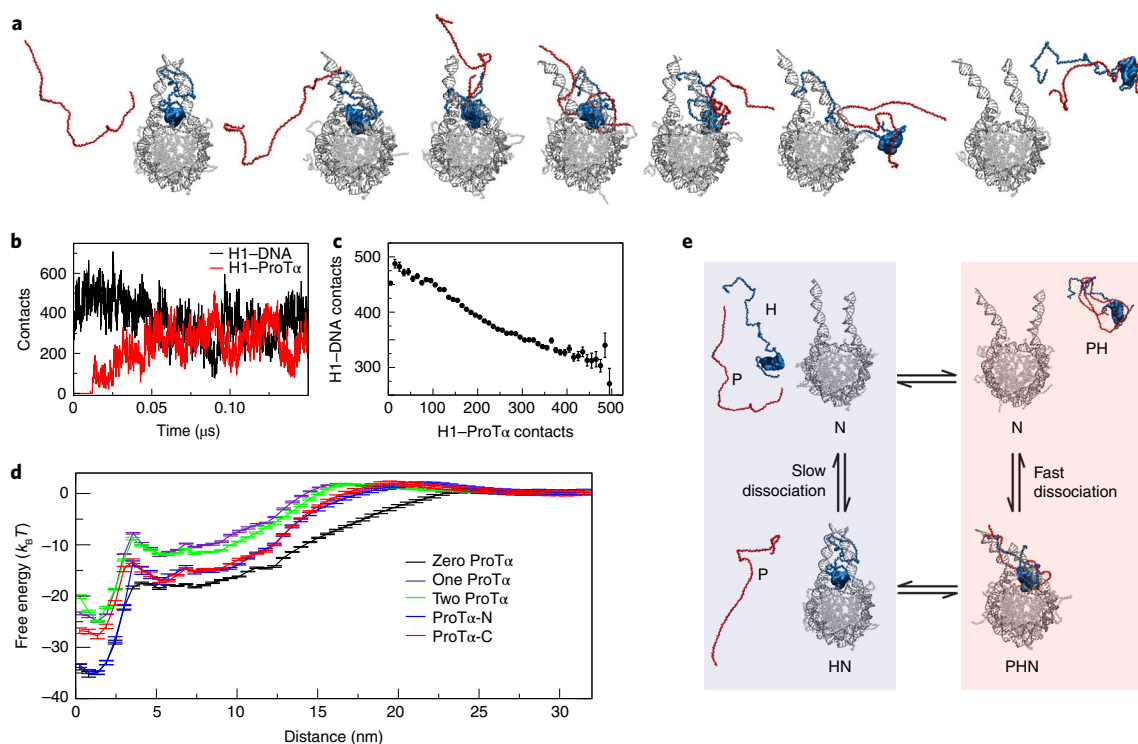


Fig. 5 | Mechanism of H1 chaperoning on the nucleosome by ProT α . **a**, Structural model based on simulation snapshots depicting the association of ProT α (red) to the H1-nucleosome complex followed by the dissociation of ProT α -H1 from the nucleosome (Supplementary Video 1). **b,c**, Formation of H1-ProT α contacts and correlated breaking of H1-DNA contacts as ProT α invades the H1-DNA complex. Error bars in **c** are standard errors of the mean number of H1-DNA contacts for each bin in H1-ProT α contacts, with the bin width being ten contacts. **d**, Potentials of mean force for unbinding of H1 from the nucleosome (distance is between the globular domain and the DNA residues it binds in the natively bound state), in the presence or absence of ProT α or its fragments (legend). ProT α -N/ProT α -C, N/C-terminal halves of ProT α . **e**, Kinetic scheme depicting the relevant molecular states. H1 (H) binds to the nucleosome (N) rapidly (forming HN), leading to compaction of the C-terminal tail of H1 and a closing of the linker DNA. H1 dissociates extremely slowly from the nucleosome by itself, but binding of ProT α (P) to H1 on the nucleosome results in a ternary complex (PHN) that facilitates dissociation of H1 from the nucleosome in the ProT α -H1 complex (PH).

molecular distances from single-molecule FRET experiments. We created constructs with labelling sites on the nucleosomal DNA, both in positions corresponding to the linker DNA and in the core particle, and along the H1 sequence (Fig. 4b, Supplementary Fig. 5c,d and Supplementary Table 2). Intermolecular FRET experiments using alternating excitation of donor and acceptor indicate 1:1 H1-nucleosome complexes under our experimental conditions (Supplementary Fig. 6), in accord with previous results²⁸. Most of the resulting transfer efficiency histograms exhibit a single peak, as expected from the rapid conformational averaging within the complex observed by nsFCS (Fig. 4c)⁵³. The similarity of the transfer efficiencies involving positions of the labels on the entry and exit linker DNA that are rotationally symmetric with respect to the dyad axis attests to the robustness of the results.

The conformational ensembles resulting from the optimized simulation model show good agreement with the measured FRET efficiencies and other experimental data. In the H1-bound state, the characteristic pattern of transfer efficiencies for different labelling positions along the H1 and DNA sequences are described remarkably well by this simple model (Fig. 4c and Supplementary Fig. 7), and even the absolute efficiency values show excellent overall agreement (concordance correlation coefficient, 0.96; Fig. 4d). The simulations also reproduce the increase in FRET efficiency between the labelled linker DNA arms observed experimentally upon binding of H1 (Fig. 4c and Supplementary Fig. 5c,d), in accord with electron cryo-microscopy results showing a compaction of the nucleosome and crossing of the linker DNA arms when H1 is bound²⁹.

In some cases, reproducible broadening or double peaks were observed in the transfer efficiency histograms (Fig. 4b), especially if the labels were located close to the exit and entry points of the nucleosomal DNA and to the globular domain of H1. We hypothesized that they are caused by the different orientations of the H1 globular domain on the dyad that were previously identified by crosslinking experiments and are expected to interconvert slowly^{14,15,29}. Indeed, when the simulations were performed with the globular domain of H1 rotated by 180° on the dyad compared to the crystal structure²⁹, the FRET efficiencies of several of the secondary populations could be reproduced (Fig. 4c). Explicitly including a representation of the fluorophores in the simulations yielded very similar results (Supplementary Fig. 7). Overall, these findings indicate that this coarse-grained, charge-dominated description of the disordered regions of H1 on the nucleosome captures the essential conformational and dynamic properties of the ensemble and further supports the notion that H1 retains its disorder when bound to the nucleosome^{7,29,58}. Figure 4e,f and Supplementary Video 1 illustrate the broad range of conformations that are populated in the H1-nucleosome complex.

Disorder underlies the mechanism of histone chaperoning. The disorder and the large-amplitude conformational fluctuations of the positively charged regions of H1 on the nucleosome suggest a simple mechanism for its displacement by the negatively charged chaperone ProT α via the multivalent interactions possible in such a complex (Fig. 5a): initial contacts between ProT α and H1 are formed in a fly-casting-like process⁵⁹, during which the number of

contacts between the two proteins progressively increases owing to the favourable electrostatic interactions. As a result, ProT α competes with the DNA for the disordered regions of H1 (Fig. 5b) and reduces the number of H1–DNA contacts (Fig. 5c) and thus the interaction strength of H1 with the nucleosome, leading to an opening of the linker DNA arms (Fig. 5a and Supplementary Video 2).

Unlike the essentially barrierless competitive substitution in polyelectrolyte complexes that occurs when the invading chain is longer and more charged than the one it is displacing²³, spontaneous dissociation of H1 was too slow to be observed on the timescale of the simulations, likely because of the much smaller charge on ProT α compared with the nucleosome. We therefore performed umbrella sampling simulations to obtain potentials of mean force for the interaction of H1 with the nucleosome in the absence and presence of ProT α (Fig. 5d); these show barrierless binding of H1 in all cases, consistent with the diffusion-limited association (Fig. 2d and Supplementary Table 1) and the similarity in salt concentration dependences of k_{off} and K_{D} (Supplementary Fig. 3) observed experimentally. The resulting binding free energy is reduced from $-38k_{\text{B}}T$ to $-28k_{\text{B}}T$ by ProT α , where k_{B} is the Boltzmann constant and T is temperature. Since the difference in K_{D} is expected to be dominated by k_{off} , this change corresponds to a pronounced increase in dissociation rate, as observed experimentally (Fig. 3 and Supplementary Fig. 3). Simulations using the N- and C-terminal halves of ProT α individually suggest that the C-terminal part of the protein makes a larger contribution to H1 dissociation, as expected from the higher charge density in this region^{6,25}. Furthermore, addition of a second ProT α does not appreciably alter the potential of mean force (Fig. 5d), supporting our use of a kinetic model in which binding of a single ProT α molecule explains the experimentally observed increase in dissociation rate (Fig. 3b).

Discussion

Our results suggest that disordered proteins can facilitate a remarkable mechanism of molecular competition: highly disordered, electrostatically driven biomolecular complexes aid the formation of transient ternary interactions, where a competing binding partner invades an existing complex and accelerates dissociation. This mechanism of ‘competitive substitution’ has been known in the field of synthetic polyelectrolytes²³, but its role in biology has largely remained unexplored. Given the great abundance of disorder in nuclear proteins, including transcriptional regulators, polymerases and other RNA- and DNA-binding factors⁴, competitive substitution is likely to be widespread among biomolecular interactions in the nucleus and may play an important role in cellular regulation.

Several lines of evidence indicate that ProT α is also an important effector in vivo. First, ProT α has been shown to increase H1 mobility in cells²⁰; second, the tens-of-micromolar ProT α concentrations reported in cells⁴⁴ correspond to the range of concentrations where we observe strong effects on H1–nucleosome affinity; and finally, the facilitated H1 dissociation we observe is a large effect and robust to salt concentration (Supplementary Fig. 3). Correspondingly, variations in ProT α concentration, for example during the cell cycle⁶⁰, may be involved in regulating H1 association with chromatin. We note that from our experimental data, we cannot exclude the possibility that multiple molecules of ProT α participate in the detachment of H1 from the nucleosome. However, the difference between the potentials of mean force from simulations with one and two ProT α molecules is negligible (Fig. 5d), suggesting no additional effect on the dissociation rate. Recent results demonstrated the formation of H1–ProT α_2 trimers in the presence of a large excess of ProT α at high micromolar concentrations⁴³, which may contribute to shifting the equilibrium, even if the trimers form only after dissociation of the H1–ProT α complex from the nucleosome.

Another observation is noteworthy: the affinity of H1 to free DNA of the length of our linker DNA or the entire nucleosomal DNA

is about two orders of magnitude lower (Supplementary Fig. 5) than the affinity of H1 to intact nucleosomes (Fig. 1), probably at least in part owing to the spatial arrangement of the DNA in the nucleosome and the more specific interactions of the globular domain at the dyad^{29,34,61}. As a result, ProT α is expected to efficiently prevent non-specific binding of H1 to DNA and ensure its targeting to the nucleosomal dyad. However, a multitude of contributions are likely to modulate the interaction of H1 with chromatin, such as other histone chaperones¹⁹, DNA-interacting machinery⁴ or local variations in ion concentrations. Proteins that compete with H1 for binding to the nucleosome, ranging from transcription factors to the high-mobility group chromatin remodelers, will also contribute to enhanced mobility of H1 in vivo⁶². In addition, post-translational modifications^{13,63} are expected to have an important effect on the interaction of H1 with the nucleosome and ProT α by fine-tuning their affinities.

Even though the existence of charged disordered regions in proteins has been known for decades, we are only now starting to elucidate the physical basis underlying their functions. Established concepts regarding the physical chemistry of polyelectrolyte interactions and the competition with inorganic ions will be essential for a detailed thermodynamic understanding of the affinities of charged IDPs and their strong sensitivity to other organic and biomolecular ions present in the cell^{13,32,33,64}. The physical properties of the charged disordered regions of H1 and the core histones are also likely to be crucial for processes involving liquid–liquid phase separation in chromatin^{10,11,18,65}. Phase separation is often driven by weak, multivalent interactions between disordered proteins and nucleic acids. The highly charged C-terminal tail of H1 has already been established to promote phase separation in chromatin, with the disordered regions allowing for multivalent interactions between nucleosomes¹⁸. The highly disordered nature of H1 on the nucleosome that emerges from our results therefore provides a plausible basis for these interactions to occur. Phase separation may be regulated further by chaperones such as ProT α or by post-translational modifications, for example phosphorylation, which has been shown to reduce the formation of H1–DNA condensates⁷.

Finally, it is worth emphasizing that our results suggest that two long-standing questions in the chromatin field, namely the nature of the structural ensemble of H1 on the nucleosome¹⁰ and the discrepancy between the residence times of H1 in vivo³⁹ and in vitro⁴⁰, are closely connected: it may be precisely the large degree of structural disorder and long-range dynamics in the tails of nucleosome-bound H1 that enable chaperones such as ProT α to invade the H1–nucleosome complex via electrostatic interactions and in this way accelerate H1 dissociation by competitive substitution instead of passively scavenging H1 once dissociated. Related processes involving charged disordered proteins may affect many aspects of chromatin assembly and dynamics, and cellular regulation in general^{11,30,65}.

Online content

Any methods, additional references, Nature Research reporting summaries, source data, extended data, supplementary information, acknowledgements, peer review information; details of author contributions and competing interests; and statements of data and code availability are available at <https://doi.org/10.1038/s41557-021-00839-3>.

Received: 22 August 2020; Accepted: 19 October 2021;

References

1. Habchi, J., Tompa, P., Longhi, S. & Uversky, V. N. Introducing protein intrinsic disorder. *Chem. Rev.* **114**, 6561–6588 (2014).
2. Watson, M. & Stott, K. Disordered domains in chromatin-binding proteins. *Essays Biochem.* **63**, 147–156 (2019).
3. Wright, P. E. & Dyson, H. J. Intrinsically disordered proteins in cellular signalling and regulation. *Nat. Rev. Mol. Cell Biol.* **16**, 18–29 (2014).

4. Fuxreiter, M. et al. Malleable machines take shape in eukaryotic transcriptional regulation. *Nat. Chem. Biol.* **4**, 728–737 (2008).
5. Vuzman, D. & Levy, Y. Intrinsically disordered regions as affinity tuners in protein–DNA interactions. *Mol. Biosyst.* **8**, 47–57 (2012).
6. Borgia, A. et al. Extreme disorder in an ultrahigh-affinity protein complex. *Nature* **555**, 61–66 (2018).
7. Turner, A. L. et al. Highly disordered histone H1–DNA model complexes and their condensates. *Proc. Natl Acad. Sci. USA* **115**, 11964–11969 (2018).
8. Srivastava, S. & Tirrell, M. V. Polyelectrolyte complexation. *Adv. Chem. Phys.* **161**, 499–544 (2016).
9. van der Gucht, J., Spruijt, E., Lemmers, M. & Cohen Stuart, M. A. Polyelectrolyte complexes: bulk phases and colloidal systems. *J. Colloid Interface Sci.* **361**, 407–422 (2011).
10. Gibbs, E. B. & Kriwacki, R. W. Linker histones as liquid-like glue for chromatin. *Proc. Natl Acad. Sci. USA* **115**, 11868–11870 (2018).
11. Larson, A. G. et al. Liquid droplet formation by HP1 α suggests a role for phase separation in heterochromatin. *Nature* **547**, 236–240 (2017).
12. Schuler, B. et al. Binding without folding – the biomolecular function of disordered polyelectrolyte complexes. *Curr. Opin. Struct. Biol.* **60**, 66–76 (2019).
13. Korolev, N., Allahverdi, A., Lyubartsev, A. P. & Nordenskiöld, L. The polyelectrolyte properties of chromatin. *Soft Matter* **8**, 9322–9333 (2012).
14. Hergeth, S. P. & Schneider, R. The H1 linker histones: multifunctional proteins beyond the nucleosomal core particle. *EMBO Rep.* **16**, 1439–1453 (2015).
15. Cutter, A. R. & Hayes, J. J. A brief review of nucleosome structure. *FEBS Lett.* **589**, 2914–2922 (2015).
16. Öztürk, M. A., De, M., Cojocaru, V. & Wade, R. C. Chromatosome structure and dynamics from molecular simulations. *Annu. Rev. Phys. Chem.* **71**, 101–119 (2020).
17. Willcockson, M. A. et al. H1 histones control the epigenetic landscape by local chromatin compaction. *Nature* **589**, 293–298 (2021).
18. Gibson, B. A. et al. Organization of chromatin by intrinsic and regulated phase separation. *Cell* **179**, 470–484, e421 (2019).
19. Flanagan, T. W. & Brown, D. T. Molecular dynamics of histone H1. *Biochim. Biophys. Acta* **1859**, 468–475 (2016).
20. George, E. M. & Brown, D. T. Prothymosin α is a component of a linker histone chaperone. *FEBS Lett.* **584**, 2833–2836 (2010).
21. Gomez-Marquez, J. & Rodríguez, P. Prothymosin α is a chromatin-remodelling protein in mammalian cells. *Biochem. J.* **333**, 1–3 (1998).
22. Karetsou, Z. et al. Prothymosin α modulates the interaction of histone H1 with chromatin. *Nucleic Acids Res.* **26**, 3111–3118 (1998).
23. Peng, B. & Muthukumar, M. Modeling competitive substitution in a polyelectrolyte complex. *J. Chem. Phys.* **143**, 243133 (2015).
24. Mao, A. H., Crick, S. L., Vitalis, A., Chicoine, C. L. & Pappu, R. V. Net charge per residue modulates conformational ensembles of intrinsically disordered proteins. *Proc. Natl Acad. Sci. USA* **107**, 8183–8188 (2010).
25. Müller-Späh, S. et al. Charge interactions can dominate the dimensions of intrinsically disordered proteins. *Proc. Natl Acad. Sci. USA* **107**, 14609–14614 (2010).
26. Lowary, P. T. & Widom, J. New DNA sequence rules for high affinity binding to histone octamer and sequence-directed nucleosome positioning. *J. Mol. Biol.* **276**, 19–42 (1998).
27. Fang, H., Clark, D. J. & Hayes, J. J. DNA and nucleosomes direct distinct folding of a linker histone H1 C-terminal domain. *Nucleic Acids Res.* **40**, 1475–1484 (2012).
28. White, A. E., Hieb, A. R. & Luger, K. A quantitative investigation of linker histone interactions with nucleosomes and chromatin. *Sci. Rep.* **6**, 19122 (2016).
29. Bednar, J. et al. Structure and dynamics of a 197 bp nucleosome in complex with linker histone H1. *Mol. Cell* **66**, 384–397.e8 (2017).
30. Sridhar, A. et al. Emergence of chromatin hierarchical loops from protein disorder and nucleosome asymmetry. *Proc. Natl Acad. Sci. USA* **117**, 7216–7224 (2020).
31. Syed, S. H. et al. Single-base resolution mapping of H1–nucleosome interactions and 3D organization of the nucleosome. *Proc. Natl Acad. Sci. USA* **107**, 9620–9625 (2010).
32. Record, M. T. Jr, Anderson, C. F. & Lohman, T. M. Thermodynamic analysis of ion effects on the binding and conformational equilibria of proteins and nucleic acids: the roles of ion association or release, screening, and ion effects on water activity. *Q. Rev. Biophys.* **11**, 103–178 (1978).
33. Anderson, C. F. & Record, M. T. Jr. Salt-nucleic acid interactions. *Annu. Rev. Phys. Chem.* **46**, 657–700 (1995).
34. Brown, D. T., Izard, T. & Misteli, T. Mapping the interaction surface of linker histone H1^o with the nucleosome of native chromatin *in vivo*. *Nat. Struct. Mol. Biol.* **13**, 250–255 (2006).
35. Gansen, A. et al. High precision FRET studies reveal reversible transitions in nucleosomes between microseconds and minutes. *Nat. Commun.* **9**, 4628 (2018).
36. Gansen, A. et al. Nucleosome disassembly intermediates characterized by single-molecule FRET. *Proc. Natl Acad. Sci. USA* **106**, 15308–15313 (2009).
37. Gopich, I. V. & Szabo, A. Decoding the pattern of photon colors in single-molecule FRET. *J. Phys. Chem. B* **113**, 10965–10973 (2009).
38. Lever, M. A., Th'ng, J. P., Sun, X. & Hendzel, M. J. Rapid exchange of histone H1.1 on chromatin in living human cells. *Nature* **408**, 873–876 (2000).
39. Misteli, T., Gunjan, A., Hock, R., Bustin, M. & Brown, D. T. Dynamic binding of histone H1 to chromatin in living cells. *Nature* **408**, 877–881 (2000).
40. Bednar, J., Hamiche, A. & Dimitrov, S. H1–nucleosome interactions and their functional implications. *Biochim. Biophys. Acta* **1859**, 436–443 (2015).
41. Bryan, L. C. et al. Single-molecule kinetic analysis of HP1–chromatin binding reveals a dynamic network of histone modification and DNA interactions. *Nucleic Acids Res.* **45**, 10504–10517 (2017).
42. Papamarcaki, T. & Tsolas, O. Prothymosin α binds to histone H1 *in vitro*. *FEBS Lett.* **345**, 71–75 (1994).
43. Sottini, A. et al. Polyelectrolyte interactions enable rapid association and dissociation in high-affinity disordered protein complexes. *Nat. Commun.* **11**, 5736 (2020).
44. Haritos, A. A., Salvin, S. B., Blacher, R., Stein, S. & Horecker, B. L. Parathymosin alpha: a peptide from rat tissues with structural homology to prothymosin alpha. *Proc. Natl Acad. Sci. USA* **82**, 1050–1053 (1985).
45. Chen, T. Y., Cheng, Y. S., Huang, P. S. & Chen, P. Facilitated unbinding via multivalency-enabled ternary complexes: new paradigm for protein–DNA interactions. *Acc. Chem. Res.* **51**, 860–868 (2018).
46. Gibb, B. et al. Concentration-dependent exchange of replication protein A on single-stranded DNA revealed by single-molecule imaging. *PLoS ONE* **9**, e87922 (2014).
47. Kamar, R. I. et al. Facilitated dissociation of transcription factors from single DNA binding sites. *Proc. Natl Acad. Sci. USA* **114**, E3251–E3257 (2017).
48. Lewis, J. S. et al. Single-molecule visualization of fast polymerase turnover in the bacterial replisome. *eLife* **6**, e23932 (2017).
49. Potoyan, D. A., Zheng, W. H., Komives, E. A. & Wolynes, P. G. Molecular stripping in the NF- κ B/I κ B/DNA genetic regulatory network. *Proc. Natl Acad. Sci. USA* **113**, 110–115 (2016).
50. Wu, H., Dalal, Y. & Papoian, G. A. Binding dynamics of disordered linker histone H1 with a nucleosomal particle. *J. Mol. Biol.* **433**, 166881 (2021).
51. Fang, H., Wei, S., Lee, T. H. & Hayes, J. J. Chromatin structure-dependent conformations of the H1 CTD. *Nucleic Acids Res.* **44**, 9131–9141 (2016).
52. Soranno, A. et al. Quantifying internal friction in unfolded and intrinsically disordered proteins with single-molecule spectroscopy. *Proc. Natl Acad. Sci. USA* **109**, 17800–17806 (2012).
53. Nettels, D., Gopich, I. V., Hoffmann, A. & Schuler, B. Ultrafast dynamics of protein collapse from single-molecule photon statistics. *Proc. Natl. Acad. Sci. USA* **104**, 2655–2660 (2007).
54. Kenzaki, H. & Takada, S. Partial unwrapping and histone tail dynamics in nucleosome revealed by coarse-grained molecular simulations. *PLoS Comput. Biol.* **11**, e1004443 (2015).
55. Zhang, B., Zheng, W., Papoian, G. A. & Wolynes, P. G. Exploring the free energy landscape of nucleosomes. *J. Am. Chem. Soc.* **138**, 8126–8133 (2016).
56. Holmstrom, E. D., Liu, Z. W., Nettels, D., Best, R. B. & Schuler, B. Disordered RNA chaperones can enhance nucleic acid folding via local charge screening. *Nat. Commun.* **10**, 245 (2019).
57. Korolev, N., Fan, Y., Lyubartsev, A. P. & Nordenskiöld, L. Modelling chromatin structure and dynamics: status and prospects. *Curr. Opin. Struct. Biol.* **22**, 151–159 (2012).
58. Lu, X., Hamkalo, B., Parseghian, M. H. & Hansen, J. C. Chromatin condensing functions of the linker histone C-terminal domain are mediated by specific amino acid composition and intrinsic protein disorder. *Biochemistry* **48**, 164–172 (2009).
59. Shoemaker, B. A., Portman, J. J. & Wolynes, P. G. Speeding molecular recognition by using the folding funnel: the fly-casting mechanism. *Proc. Natl Acad. Sci. USA* **97**, 8868–8873 (2000).
60. Vareli, K., Tsolas, O. & Frangou-Lazaridis, M. Regulation of prothymosin α during the cell cycle. *Eur. J. Biochem.* **238**, 799–806 (1996).
61. Wang, S. et al. Linker histone defines structure and self-association behaviour of the 177 bp human chromatosome. *Sci. Rep.* **11**, 380 (2021).
62. Catez, F., Ueda, T. & Bustin, M. Determinants of histone H1 mobility and chromatin binding in living cells. *Nat. Struct. Mol. Biol.* **13**, 305–310 (2006).
63. Annalisa, I. & Robert, S. The role of linker histone H1 modifications in the regulation of gene expression and chromatin dynamics. *Biochim. Biophys. Acta* **1859**, 486–495 (2015).
64. Privalov, P. L., Dragan, A. I. & Crane-Robinson, C. Interpreting protein/DNA interactions: distinguishing specific from non-specific and electrostatic from non-electrostatic components. *Nucleic Acids Res.* **39**, 2483–2491 (2011).
65. Shakyia, A., Park, S., Rana, N. & King, J. T. Liquid-liquid phase separation of histone proteins in cells: role in chromatin organization. *Biophys. J.* **118**, 753–764 (2020).

Publisher's note Springer Nature remains neutral with regard to jurisdictional claims in published maps and institutional affiliations.

© The Author(s), under exclusive licence to Springer Nature Limited 2021

Methods

Protein preparation and labelling. Recombinant wild-type human histone H1.0 (H1; New England Biolabs, catalog no. M2501S) was used for experiments with fluorescently labelled nucleosomes. ProTα was prepared as previously described²⁵. Variants of H1 for fluorescent labelling were produced by bacterial expression using a modified version of the pRSET vector⁶⁶ containing the human H1F0 gene (UniProt P07305), a hexahistidine tag and a thrombin cleavage site⁶. All protein variants were confirmed to have the correct molecular weight by mass spectrometry. Cysteine mutations were introduced for labelling the protein with fluorescent dyes using site-directed mutagenesis. H1 variants were expressed, purified and fluorescently labelled as previously described⁶. Briefly, all H1 variants were expressed in *Escherichia coli* C41 cells in terrific broth medium at 37 °C, using isopropylthiogalactopyranoside (IPTG) to induce expression. The cells were pelleted after three hours of growth, resuspended in denaturing buffer containing 6 M guanidinium chloride (GdmCl) and had the soluble fraction applied to a Ni-IDA resin (Agarose Bead Technologies). After washing, the protein was eluted using 250–500 mM imidazole, then dialysed against phosphate-buffered saline (PBS), followed by thrombin (Serva) cleavage to remove the hexahistidine tag. The uncleaved protein and cleaved hexahistidine tag were removed from the eluted mixture with a HisTrap HP 5 ml column (GE Healthcare) in PBS with 25 mM imidazole. The final purification step was performed by anion exchange chromatography using a Mono S column (GE Healthcare). Before fluorescent labelling, samples were reduced with dithiothreitol (DTT) and purified by reversed-phase high-performance liquid chromatography (RP-HPLC) using a Repronil-Gold C4 column. H1-containing fractions were resuspended and labelled in denaturing buffer (6 M GdmCl, 50 mM sodium phosphate, pH 7.0), before a final RP-HPLC purification step. Lyophilized proteins were resuspended in 8 M GdmCl, frozen in liquid nitrogen and stored at –80 °C. All experiments were performed in TEK buffer (10 mM Tris, 0.1 mM EDTA, pH 7.4) at different salt concentrations adjusted by addition of KCl. Protein sequences and labelling positions are shown in Supplementary Table 2. The dye pairs Alexa Fluor 488/Alexa Fluor 594 (Förster radius $R_0 = 5.4$ nm) and Cy3B/CF660R ($R_0 = 6.0$ nm) were used for experiments with freely diffusing molecules and for surface-immobilized nucleosomes, respectively.

Preparation of fluorescently labelled oligonucleotides. A ~10 μl solution of 5–10 nmol oligonucleotide (thymine modified with a C6-amino linker for the reaction with the succinimidyl ester of the fluorescent dye; Integrated DNA Technologies; Supplementary Table 2) was diluted with 50 μl labelling buffer (0.1 M sodium bicarbonate, pH 8.3). For analytical purposes, a 1 μl sample was diluted with 50 μl of RP-HPLC solvent A (95% 0.1 M triethylammonium acetate, 5% acetonitrile), followed by RP-HPLC using a Repronil-Pur 200 5 μm, 250 × 4 mm C18 column (Dr. Maisch) using a gradient of 0–100% RP-HPLC solvent B (100% acetonitrile) in 50 minutes. Then 50–100 μg fluorescent dye succinimidyl ester (Cy3B/CF660R) dissolved in dimethylsulfoxide was sonicated for 10 minutes and added to the oligonucleotide solution in labelling buffer and the reaction incubated at room temperature for at least two hours. After ethanol precipitation to remove excess dye, the pelleted oligonucleotide was redissolved in 100 μl, 95% A, 5% B RP-HPLC solvent. Labelled oligonucleotides were purified using the same column and gradient as above, lyophilized and resuspended in double-distilled water (ddH₂O) to a final concentration of 2.5 μM and stored at –20 °C. The correct molecular weights of the labelled oligonucleotides were confirmed by mass spectrometry.

Preparation of core-histone octamer. Human wild-type core histones (H2A, H2B, H3, H4) were prepared as previously described⁶⁷. Each core-histone protein was expressed in BL21 DE3 pLysS cells using a pET3a plasmid carrying the corresponding gene. Cells were grown at 37 °C in LB media including 100 μg ml⁻¹ ampicillin and 35 μg ml⁻¹ chloramphenicol until an optical density of 0.6 at a wavelength of 600 nm (OD₆₀₀) was reached, at which point protein expression was induced by addition of IPTG to a final concentration of 0.5 mM. The cells were harvested 3 hours after induction, the cell pellets resuspended in lysis buffer (20 mM Tris, 1 mM EDTA, 200 mM NaCl, 1 mM 2-mercaptoethanol (2-ME), one cOmplete Protease Inhibitor Cocktail tablet (Roche) per 50 ml, pH 7.5), followed by cell lysis by freeze–thawing and sonication. The inclusion body pellet was washed three times with the histone lysis buffer (twice with and once without 1% Triton X-100). The histones were resolubilized in histone resolubilization buffer (6 M GdmCl, 20 mM Tris, 1 mM EDTA, 1 mM 2-ME, pH 7.5) and then dialysed against urea buffer (7 M urea, 10 mM Tris, 1 mM EDTA, 0.1 M NaCl, 5 mM 2-ME, pH 7.5). The proteins were then purified by cation exchange using a 5 ml HiTrap SP HP column (GE Healthcare) and the collected fractions analysed by sodium dodecyl sulphate polyacrylamide gel electrophoresis. The final purification step was performed by preparative RP-HPLC on a Zorbax 300SB 7 μm 21.2 × 250 mm column using a gradient of 30–70% solvent B (A, water with 0.1% trifluoroacetic acid (TFA); B, 9.9% water, 90% acetonitrile with 0.1% TFA). The collected fractions were characterized by analytical RP-HPLC and electrospray ionization mass spectrometry, lyophilized and stored at –20 °C.

To refold the core-histone octamer, 0.4–1.5 mg of each of the purified lyophilized human histones were dissolved in 6 M GdmCl, 10 mM Tris and 5 mM

DTT, pH 7.5, and the protein concentrations quantified by UV absorbance. Equimolar amounts of H3 and H4 were mixed with 1.05 equivalents of H2A and H2B to a final concentration of 1 mg ml⁻¹, and octamers were refolded by dialysing against 2 M NaCl, 10 mM Tris, 1 mM EDTA and 5 mM DTT, pH 7.5. The refolded octamers were then purified by gel filtration on a Superdex S200 10/300GL column (GE Healthcare) and the collected fractions analysed by sodium dodecyl sulphate polyacrylamide gel electrophoresis. The octamer-containing fractions were pooled and concentrated to ~50 μM; glycerol was added to a final concentration of 50% (v/v) and the samples stored at –20 °C.

PCR amplification of 197-bp DNA containing the 601 Widom sequence.

DNA for nucleosome reconstitution was generated by PCR amplification of a pJ201 plasmid template containing the 147-bp Widom sequence⁶⁸, either with unlabelled oligonucleotides (Integrated DNA Technologies) or fluorescently labelled oligonucleotides (as described in the Preparation of fluorescently labelled oligonucleotides section). DNA for nucleosomes for surface immobilization was generated by using oligonucleotides with a modified thymidine containing a C6-amino linker and a biotin moiety (Integrated DNA Technologies). The oligonucleotides were designed so that the Widom sequence was extended by a linker DNA of 25-bp length on either side. PCR was typically performed in 10 × 50 μl volume by mixing in PCR tubes Phusion HF buffer (×1, New England Biolabs), plasmid template (0.02 ng μl⁻¹), 0.25 μM forward primer, 0.25 μM reverse primer and deoxynucleotide triphosphates (dNTPs, 0.2 mM each) with ddH₂O and 1.0 units of Phusion high-fidelity DNA polymerase (New England Biolabs). Thermocycles included 30 s for initial denaturation at 94 °C, followed by 30 cycles of 20 s for denaturation at 94 °C, 10 s for annealing at 66 °C and 15 s for extension at 72 °C. The completed PCR reactions were pooled and ethanol-precipitated prior to purification using a DNA Clean and Concentrator Kit (DCC-25, Zymo Research). The concentration of the labelled 197-bp PCR products was determined by UV absorbance. DNA sequences of the 197-nucleotide α and β strands containing the 601 Widom sequence, primer sequences and positions of nucleotides that were modified for labelling or biotinylation are listed in Supplementary Table 2.

Nucleosome reconstitution. Nucleosomes were reconstituted⁶⁹ using 10 pmol of purified DNA containing the 147-bp 601 Widom sequence⁶⁸ flanked by 25-bp linkers. The DNA was mixed with 0.9–1.5 molar equivalents of recombinant core-histone octamer at a final concentration of 2 M NaCl on ice. The 30 μl reaction was then transferred to a Slide-A-Lyzer MINI dialysis device (Thermo Fisher Scientific) and dialysed against a linear gradient of buffer with decreasing salt concentration, starting from 10 mM Tris, 0.1 mM EDTA and 2 M KCl, pH 7.5 to 10 mM Tris, 0.1 mM EDTA and 10 mM KCl, pH 7.5, over ~20 hours. The gradient was created by slowly removing buffer from the dialysis container with a constant flow rate using a peristaltic pump and, simultaneously, supplying fresh buffer with 10 mM KCl using the same flow rate and thus keeping the volume constant. The reactions were then transferred to microcentrifuge tubes and centrifuged for 5 min at 21,000g and 4 °C to remove aggregates; the supernatant was transferred to a new tube. After determining the volumes and concentrations of the samples via absorbance at 260 nm, 0.2–0.5 pmol of the reaction products were loaded on a 6% agarose gel (Invitrogen) and run for 90 min at 90 V with ×0.25 Tris–borate as running buffer. The gels were stained with GelRed (Biotium) for 30 minutes and visualized under UV light. Only nucleosome preparations containing less than 5% of free DNA in the sample were used for measurements.

Surface immobilization of nucleosomes. Quartz coverslips coated with polyethylene glycol and biotin (MicroSurfaces) were sonicated in Tween-20 (Thermo Fisher Scientific) and extensively washed with ddH₂O before binding to silicone hybridization chambers (SecureSeal hybridization chambers, Grace BioLabs), forming chambers with a sample volume of 150 μl. The chambers were washed several times with 50 mM sodium phosphate buffer containing 0.01% Tween-20 and then incubated with a 1 μM neutravidin solution (Vector Labs) for 10 minutes. After three washing steps with TEK buffer including 0.01% Tween-20, the chambers were filled with a 10 to 20 pM solution of biotinylated and fluorescently labelled nucleosomes in TEK buffer with 0.1 mg ml⁻¹ bovine serum albumin (BSA) and 0.01% Tween-20 for 5–10 minutes, followed by another two washing steps in TEK buffer. The agreement between data taken on surface-immobilized and freely diffusing molecules with and without BSA, respectively (Fig. 1d), indicates that despite its negative charge, BSA does not interfere with the H1–nucleosome interactions. The transfer efficiency and binding affinity of the H1–nucleosome complex were also tested explicitly using freely diffusing molecules in the presence and absence of BSA, and were found to be unaffected.

Single-molecule fluorescence spectroscopy. Single-molecule experiments on freely diffusing molecules were conducted at 22 °C using either a custom-built confocal instrument or a MicroTime 200 (PicoQuant), including a HydraHarp 400 time-correlated single-photon counting module (PicoQuant). The donor dye was excited using a 485 nm diode laser at 100 μW power (measured at the back aperture of the objective), either in continuous-wave mode or with pulsed interleaved excitation⁷⁰ to enable alternating excitation of donor and acceptor dyes.

For acceptor excitation, the light from a supercontinuum laser (NKT Photonics) operating at 20 MHz repetition rate was passed through a z582/15 band-pass filter (Chroma) and adjusted to an average power of 35 μW at the back aperture of the objective. Excitation and emission light was focused and collected, respectively, using a high-numerical-aperture microscope objective (Olympus UPlanApo $\times 60/1.20\text{W}$). Emitted fluorescence was focused onto a 100 μm pinhole and separated into four detection channels by polarization and donor and acceptor emission wavelengths. Single-photon avalanche diodes were used for detection (SPCM-AQR-15, PerkinElmer, or τ -SPADs, PicoQuant). All experiments involving freely diffusing molecules were performed in μ -Slide sample chambers (Ibidi) at 22 $^{\circ}\text{C}$ in TEK buffer with varying KCl concentrations of 150–400 mM (the salt concentrations quoted throughout the manuscript include the 8 mM ionic strength of 10 mM Tris at pH 7.4); 140 mM 2-ME and 0.01% (v/v) Tween-20 were added for photoprotection and for minimizing surface adhesion, respectively.

Single-molecule experiments with surface-immobilized nucleosomes were conducted on a custom-built confocal instrument with a 532 nm continuous-wave laser (LaserBoxx LBX-532-50-COL-PP, Oxixius). The objective (UPlanApo $\times 60/1.20\text{W}$, Olympus) was mounted on a piezo stage (P-733.2 and PIFOC, Physik Instrumente) for scanning. Fluorescence emission was collected and split into two channels with a dichroic mirror (T635LPXR, Chroma). Donor emission was filtered with an ET585-65m band-pass filter (Chroma) and detected with a τ -SPAD (PicoQuant); acceptor emission was filtered with a LP647RU long-pass filter (Chroma) and detected with a SPCM-AQRH-14 single-photon avalanche diode (PerkinElmer). After surface immobilization of nucleosomes, experiments were performed by filling the reaction chamber with degassed TEK buffer containing H1 and/or ProT α , under an argon atmosphere to exclude atmospheric oxygen. The buffer contained KCl to adjust the salt concentration, 0.1 mg ml^{-1} of BSA to reduce non-specific surface interactions and D_2O instead of H_2O to increase the quantum yield of the dyes⁷¹. An oxygen scavenging system containing 2.5 mM protocatechuic acid and 1 nM protocatechuate-3,4-dioxygenase was used to improve photostability⁷², and 1 mM methyl viologen and 1 mM ascorbic acid⁷³ were used for triplet quenching and radical scavenging. A surface area of $20 \times 20 \mu\text{m}^2$ was scanned (78 nm per pixel) at a laser power of $2 \mu\text{W}$ to locate single immobilized nucleosomes. The axial position and the objective correction collar were adjusted to maximize the fluorescence intensity detected.

Data for FRET efficiency histograms from freely diffusing molecules were collected on samples containing 50–100 pM double-labelled H1 or nucleosomes; intermolecular FRET efficiencies were measured on samples with up to 500 pM of acceptor-labelled nucleosomes to ensure saturation of binding, and up to 5 nM in time-resolved FRET experiments at elevated salt concentrations (Supplementary Fig. 3). FRET efficiencies were calculated according to $E = \hat{N}_A / (\hat{N}_A + \hat{N}_D)$, where \hat{N}_D and \hat{N}_A are the number of donor and acceptor photons in a fluorescence burst, respectively, after correction for background, direct acceptor excitation, channel crosstalk, and differences in dye quantum yields and photon detection efficiencies⁷⁴. Aggregates, identified as occasional fluorescence bursts with photon counts greater than three standard deviations from the mean signal binned at 1 s, were removed before data analysis. For experiments on surface-immobilized nucleosomes, we determined photon count ratios and summed for all traces recorded at the same salt concentration and H1 concentration, which report accurately on the ratio of bound and unbound populations (even though the photon count ratio may differ from the corrected absolute transfer efficiencies).

nsFCS. Data for nsFCS^{52,75} were collected using continuous-wave excitation at 485 nm and an ~ 100 pM sample of either donor-labelled H1 with acceptor-labelled nucleosomes, or double-labelled H1 with an excess of unlabelled dsDNA or nucleosomes. Donor and acceptor fluorescence photons from the bound subpopulation were used for the correlations at 1 ns binning time. Photons were recorded with two detectors each for donor and acceptor and cross-correlated between detectors to avoid the effects of detector dead times and after-pulsing on the correlation functions. Autocorrelation curves of acceptor and donor channels and cross-correlation curves between acceptor and donor channels were fit and analysed as described previously⁶. Briefly, the correlation curves were fit over a lag time interval from $-2.5 \mu\text{s}$ to $+2.5 \mu\text{s}$ using

$$g_{ij}(\tau) = a \left(1 - c_{ab} e^{-\frac{|\tau|}{\tau_{ab}}} \right) \left(1 + c_{cd} e^{-\frac{|\tau|}{\tau_{cd}}} \right) \left(1 + c_T e^{-\frac{|\tau|}{\tau_T}} \right),$$

where i and j indicate donor (D) or acceptor (A) fluorescence emission; the amplitude a depends on the effective mean number of molecules in the confocal volume and on the background signal; c_{ab} , τ_{ab} , c_{cd} and τ_{cd} are the amplitudes and time constants of photon antibunching (ab) and chain dynamics (cd), respectively; c_T and τ_T refer to the triplet blinking component occurring on the microsecond timescale. Fluctuations in the inter-dye distance result in specific features in the correlation functions: donor and acceptor autocorrelations have a positive amplitude ($c_{cd} > 0$), whereas the donor–acceptor cross-correlation has a negative amplitude ($c_{cd} < 0$), but all correlations have identical decay times⁶. All three correlation curves were thus fit globally with the same value of τ_{cd} applied to all curves, but allowing for different values of c_{ab} , c_{cd} , τ_{ab} , τ_T and c_T as free fit parameters. τ_{cd} can be converted to the reconfiguration time of the chain, τ_r , by modelling chain

dynamics as a diffusive process in the potential of mean force derived from the sampled inter-dye distance distribution $P(r)^{75,76}$ based on the SAW- ν model^{77,78}. The correlation functions are displayed throughout the paper with a normalization to 1 at their respective values at 0.5 μs to facilitate direct comparison.

Fluorescence lifetime and fluorescence anisotropy. Fluorescence lifetimes were estimated from the mean donor (t_D) and acceptor (t_A) detection times after the excitation pulse. The average lifetimes were then combined with the transfer efficiencies in two-dimensional plots (Supplementary Fig. 6) where $\tau_D^0/\tau_D^0 = t_D/\tau_D^0$ and $\tau_A^0/\tau_A^0 = (t_A - \tau_A^0)/\tau_A^0$ were calculated for each burst. Here, τ_D^0 and τ_A^0 are the intrinsic donor and acceptor lifetimes, respectively. For a static inter-dye distance, the normalized mean fluorescence lifetimes are equal to $1 - E$ (diagonal lines in Supplementary Fig. 6), whereas systems rapidly sampling a broad distance distribution deviate from the diagonal^{79,80}.

Fluorescence anisotropies for donor and acceptor dyes were determined for all intra- and intermolecular labelling pairs from the single-molecule measurements and yielded values of 0.09–0.14 for the donor dye and 0.16–0.22 for the acceptor dye (upon direct excitation), which indicates sufficiently rapid reorientational dynamics of the dyes for approximating the orientational factor in Förster theory by 2/3 (ref. 81).

Binding affinities. Transfer efficiency histograms were recorded for either double-labelled H1 or nucleosomes with increasing concentrations of the unlabelled binding partner until no further change in transfer efficiency was observed. The histograms were fit with two or more Gaussian peak functions to quantify the relative areas of the bound and unbound subpopulations and the resulting fraction of bound species (θ). The binding isotherm (θ versus ligand concentration) was then fit to quantify the dissociation constant (K_D) using

$$\theta = \frac{c_{X,\text{tot}} + K_D + c_{Y,\text{tot}} + \sqrt{(c_{X,\text{tot}} + K_D + c_{Y,\text{tot}})^2 - 4c_{X,\text{tot}}c_{Y,\text{tot}}}}{2c_{Y,\text{tot}}},$$

where $c_{X,\text{tot}}$ and $c_{Y,\text{tot}}$ are the total concentrations of H1 or nucleosome, depending on which molecule is kept at constant concentration ($c_{X,\text{tot}}$ variable, $c_{Y,\text{tot}}$ constant). Errors on K_D values are based on pipetting error estimates, propagated through corresponding dilution steps at each salt concentration⁶. The number of counterions released upon complex formation can be estimated from the salt concentration dependence of the K_D according to the model of Record et al.⁸².

Analysis of fluorescence time traces from surface-immobilized molecules.

Single-molecule fluorescence time traces were first inspected visually, and any recordings showing pronounced changes in count rate, that is, those indicative of nucleosome unwrapping (Supplementary Fig. 1), were excluded from further analysis. These traces could furthermore be identified by a markedly increased off-rate of H1 that results in a much lower affinity than expected from the experiments using freely diffusing molecules. The trajectories of immobilized nucleosomes binding to H1 free in solution (Fig. 2a) exhibited transitions between two states: the H1-bound nucleosome with high FRET efficiency and the unbound nucleosome with low FRET efficiency, in accordance with the free-diffusion experiments (Fig. 1b,c). We therefore analysed the system in terms of a two-state model described by a rate matrix, \mathbf{K} , with transitions between unbound (N) and bound (HN) nucleosome:

$$\mathbf{K} = \begin{pmatrix} -k_{\text{on}}^{\text{HN}} & k_{\text{off}}^{\text{HN}} \\ k_{\text{on}}^{\text{HN}} & -k_{\text{off}}^{\text{HN}} \end{pmatrix},$$

where c_i is the concentration of H1 in solution, and $k_{\text{on}}^{\text{HN}}$ and $k_{\text{off}}^{\text{HN}}$ are the association and dissociation rate coefficients, respectively. The photon detection rates for donor and acceptor are estimated by applying maximum likelihood analysis to the binned time traces⁸², where the likelihood (L_m) for time trace m with bin size Δ , number of bins (T_m) and ($N_{D,t}$, $N_{A,t}$) photons detected in time bin t is calculated according to

$$L_m = 1^T \left[\prod_{t=1}^{T_m} \mathbf{F}_t e^{\mathbf{K}\Delta} \right] \mathbf{p}_{\text{eq}},$$

The population vector \mathbf{p}_{eq} describes the equilibrium distribution of states, for which $\mathbf{K}\mathbf{p}_{\text{eq}} = 0$ and $1^T \mathbf{p}_{\text{eq}} = 1$, where $1^T = (1 \ 1 \ \dots)$ is the transposed vector of ones. \mathbf{F}_t is a diagonal matrix with elements

$$(\mathbf{F}_t)_{ii} = \frac{(n_{D,t}\Delta)^{N_{D,t}}}{N_{D,t}!} e^{-n_{D,t}\Delta} \times \frac{(n_{A,t}\Delta)^{N_{A,t}}}{N_{A,t}!} e^{-n_{A,t}\Delta},$$

assuming Poisson statistics for the number of photons per bin; $n_{D,t}$ and $n_{A,t}$ are the mean photon detection rates of the i th state in the donor and acceptor channels, respectively. The photon detection rates and transition rate coefficients are then found by maximizing the sum of the logarithm of the likelihoods, $\sum_m \ln(L_m)$. Using the Viterbi algorithm^{83,84}, we also identified the most likely state trajectories using the photon detection rates and transition rate coefficients determined from the maximum likelihood analysis, and obtained the distributions of dwell times,

which yielded rate coefficients in good agreement with those obtained with the maximum likelihood analysis when fit with single-exponential decays.

For describing the kinetics in the presence of ProT α , we assume that the nucleosome can additionally be in complex with both H1 and ProT α , forming the ternary complex PHN. Accordingly, we describe the measurements (Fig. 3b) with a three-state model (including N, HN and PHN) based on the rate matrix

$$\mathbf{K}(c_P) = \begin{pmatrix} -k_{\text{on}}^{\text{HN}} c_{\text{H}} - k_{\text{on}}^{\text{PH-N}} c_{\text{PH}} & k_{\text{off}}^{\text{HN}} & k_{\text{off}}^{\text{PH-N}} \\ k_{\text{on}}^{\text{HN}} c_{\text{H}} & -k_{\text{off}}^{\text{HN}} - k_{\text{on}}^{\text{P-HN}} c_{\text{P}} & k_{\text{off}}^{\text{P-HN}} \\ k_{\text{on}}^{\text{PH-N}} c_{\text{PH}} & k_{\text{on}}^{\text{P-HN}} c_{\text{P}} & -k_{\text{off}}^{\text{P-HN}} - k_{\text{off}}^{\text{PH-N}} \end{pmatrix},$$

where c_{PH} and c_{P} are the concentrations of PH and P in solution, respectively. Even though a unique determination of all four additional rate coefficients besides the independently known $k_{\text{on}}^{\text{HN}}$ and $k_{\text{off}}^{\text{HN}}$ is not feasible based on the available data, the dependence of the observed transition rate coefficients between low- and high-FRET states on ProT α concentration can be described well with this model (solid lines in Fig. 3b) according to

$$k_{\text{off}}^{\text{obs}} = \frac{K_{\text{D},1} K_{\text{D},3} k_{\text{on}}^{\text{HN}} c_{\text{H}} (k_{\text{off}}^{\text{HN}} + k_{\text{on}}^{\text{P-HN}} c_{\text{P}})}{(c_{\text{H}} c_{\text{P}} + (c_{\text{P}} + K_{\text{D},1}) K_{\text{D},3}) k_{\text{off}}^{\text{HN}}}$$

and

$$k_{\text{on}}^{\text{obs}} = k_{\text{off}}^{\text{HN}} + c_{\text{P}} k_{\text{on}}^{\text{P-HN}},$$

showing that the formation of the ternary complex PHN can explain the observed kinetic behaviour, in contrast to a model without PHN (dashed lines in Fig. 3b).

In the ternary complex model, $K_{\text{D},1} = \frac{k_{\text{off}}^{\text{HN}}}{k_{\text{on}}^{\text{HN}}} (\text{PH} \rightleftharpoons \text{P} + \text{H})$,

$K_{\text{D},2} = \frac{k_{\text{off}}^{\text{HN}}}{k_{\text{on}}^{\text{HN}}} (\text{HN} \rightleftharpoons \text{H} + \text{N})$, $K_{\text{D},3} = \frac{k_{\text{off}}^{\text{PH-N}}}{k_{\text{on}}^{\text{PH-N}}} (\text{PHN} \rightleftharpoons \text{PH} + \text{N})$ and

$K_{\text{D},4} = \frac{k_{\text{off}}^{\text{P-HN}}}{k_{\text{on}}^{\text{P-HN}}} (\text{PHN} \rightleftharpoons \text{P} + \text{HN})$. For deriving the equations of the observed transition rate coefficients, we assumed detailed balance, which implies

$K_{\text{D},1} K_{\text{D},3} = K_{\text{D},2} K_{\text{D},4}$. We calculated $k_{\text{off}}^{\text{obs}}$ as the reciprocal mean dwell time in the low-FRET states N and PHN, and $k_{\text{on}}^{\text{obs}}$ as the reciprocal mean dwell time in the high-FRET state, that is HN. $K_{\text{D},3}$ and $k_{\text{on}}^{\text{P-HN}}$ are the only fit parameters, since $K_{\text{D},1}$ is known from Borgia et al.⁶. Interestingly, the simulations suggest that N and PHN exhibit similar inter-dye distances, and the experimental data (Fig. 3b) can indeed only be described if we assume that HN exhibits high FRET efficiency and that both N and PHN exhibit low FRET efficiency, suggesting that ProT α binding leads to the opening of the linker DNA in the H1–nucleosome complex. Intermolecular FRET experiments (Supplementary Fig. 3) demonstrate, however, that H1 dissociation from the nucleosome in the presence of ProT α occurs on a similar timescale as the transitions from high to low (E) (Fig. 3), indicating that nucleosome opening is coupled to rapid dissociation of H1 with ProT α .

Simulations. Protein model. Each residue of ProT α and the core and linker histones was represented as a bead (C-beads) mapped on the C α atom of the X-ray crystal structure (PDB no. 5NL0). The potential energy had the following functional form⁶:

$$V_{\text{Protein}} = \frac{1}{2} \sum_{i=1}^N k_b (d_i - d_i^0)^2 + \frac{1}{2} \sum_{i=1}^{N-1} k_\theta (\theta_i - \theta_i^0)^2 + \sum_{i=1}^{N-2} \sum_{m=1}^4 k_{i,m} (1 + \cos(n\phi_i - \delta_{i,m})) + \sum_{i<j} \frac{q_i q_j}{4\pi\epsilon_0 \epsilon_d d_{ij}} e^{-\frac{d_{ij}}{\lambda_D}} + \sum_{(ij) \in \text{Native}} \epsilon_{ij} \left[13 \left(\frac{\sigma_{ij}}{d_{ij}} \right)^{12} - 18 \left(\frac{\sigma_{ij}}{d_{ij}} \right)^{10} + 4 \left(\frac{\sigma_{ij}}{d_{ij}} \right)^6 \right] + \sum_{(ij) \notin \text{Native}} 4\epsilon_{\text{pp}} \left[\left(\frac{\sigma_{ij}}{d_{ij}} \right)^{12} - \left(\frac{\sigma_{ij}}{d_{ij}} \right)^6 \right]$$

The first and second terms describe bond lengths (d_i) and angles (θ_i), respectively, using harmonic potentials with force constants k_b , k_θ and equilibrium values for bond lengths (d_i^0) and angles (θ_i^0) for all N bonds assigned according to the distances and angles between C α atoms in the all-atom structure, as previously described⁸⁵; values for unstructured regions were taken from an extended conformation. The third term defines the torsions (dihedrals) between four beads linked by three bonds. The dihedral parameters (force constants $k_{i,m}$ and phase shifts $\delta_{i,m}$) were obtained from a knowledge-based potential based on the PDB⁸⁵. The fourth term describes electrostatic interactions between charged residues using a screened Coulomb potential. Aspartate and glutamate residues were assigned a charge of -1 , lysine and arginine a charge of $+1$ and histidine a charge of $+0.5$ to account for the pK $_a$ of histidine of ~ 6.5 . A charge of 0 was assigned to all the other beads. In the Coulomb term, q_i is the charge of residue i ; ϵ_0 is the permittivity of free space; and ϵ_d is the relative dielectric constant of water, which was set to a value of 80 . The Debye screening length, λ_D , is given by

$$\lambda_D = \left(\frac{\epsilon_0 \epsilon_d k_B T}{2N_A e^2 I} \right),$$

where N_A is Avogadro's constant, e is the elementary charge, I denotes the ionic strength, k_B is the Boltzmann constant and T is temperature.

The fifth and sixth terms define short-range attractive interactions between beads i and j separated by distance d_{ij} . These interactions are applied differently to disordered and folded regions of the proteins. For the folded regions, native interactions are enforced using a 12-10-6 pair potential⁸⁵. The values of ϵ_{ij} were calculated based on the globular domain of H1 and core histones according to the native-centric model of Karanicolas and Brooks⁸⁵. The coefficient σ_{ij} was set according to the C α distances in the crystal structure. For disordered regions and interactions between non-native residue pairs and the folded regions (that is, those not in contact in the native state), the ϵ_{pp} term defining the strength of the interaction between beads was tuned to the value of $0.16 k_B T$ ($\sim 0.40 \text{ kJ mol}^{-1}$), the value that was shown to produce the best agreement with the experimentally determined FRET efficiencies (Fig. 4) for the 1:1 ProT α /H1 complex⁶, while the value of $\sigma_{ij} = (\sigma_i + \sigma_j)/2$ was determined based on σ_i , specific to each residue type⁸⁶.

DNA model. The coarse-grained model of the DNA comprised three beads representing the phosphate (P), ribose (R) and base (B) moieties of a nucleotide and were mapped to the P, C4' and N1 atoms from the all-atom DNA structure, respectively. Phosphate beads were assigned a charge of -1 . The functional form of the potential for the DNA was

$$V_{\text{DNA}} = \frac{1}{2} \sum_{i<j} k_b (d_i - d_i^0)^2 + \frac{1}{2} \sum_{i<j} k_\theta (\theta_i - \theta_i^0)^2 + \sum_{i<j} \frac{q_i q_j}{4\pi\epsilon_0 \epsilon_d d_{ij}} e^{-\frac{d_{ij}}{\lambda_D}} + \sum_{(ij) \in \text{Stack}} 4\epsilon_{\text{Stack}} \left[\left(\frac{\sigma_{ij}}{d_{ij}} \right)^{12} - \left(\frac{\sigma_{ij}}{d_{ij}} \right)^6 \right] + \sum_{(ij) \in \text{Pair}} 4\epsilon_{\text{Pair}} \left[\left(\frac{\sigma_{ij}}{d_{ij}} \right)^{12} - \left(\frac{\sigma_{ij}}{d_{ij}} \right)^6 \right] + \sum_{(ij) \notin \text{Pair, Stack}} 4\epsilon_{\text{ns}} \left[\left(\frac{\sigma_{ij}}{d_{ij}} \right)^{12} - \left(\frac{\sigma_{ij}}{d_{ij}} \right)^6 \right]$$

The first two terms describe bonds and angles between beads, with parameters chosen to reproduce the equilibrium structure of B-DNA. A screened Coulomb potential was used for electrostatic interactions as described above. Non-bonded Lennard-Jones potentials were used to reproduce stacking and pairing between bases. The corresponding values of ϵ_{Stack} and ϵ_{Pair} were set to $3.0 k_B T$ ($\sim 7.5 \text{ kJ mol}^{-1}$) and $3.5 k_B T$ ($\sim 8.8 \text{ kJ mol}^{-1}$), respectively, consistent with previously estimated free energy values for base stacking⁸⁷. Interactions between DNA beads not involved in stacking or native base pairing were described by a very weakly attractive potential of $\epsilon_{\text{ns}} = 0.04 k_B T$ ($\sim 0.10 \text{ kJ mol}^{-1}$). This is the same model used previously to describe a DNA hairpin⁸⁶; only ϵ_{Pair} was optimized to obtain the persistence length ($\sim 50 \text{ nm}$) characteristic of double-helical DNA⁸⁷.

Protein–DNA interaction potential. The potential energy for the interactions between DNA and protein beads is composed of a screened Coulomb potential, which describes the interaction between charged beads, and short-range potentials:

$$V_{\text{Protein-DNA}} = \sum_{i<j} \frac{q_i q_j}{4\pi\epsilon_0 \epsilon_d d_{ij}} e^{-\frac{d_{ij}}{\lambda_D}} + \sum_{((ij) \in \text{Native})} \epsilon_{ij} \left[13 \left(\frac{\sigma_{ij}}{d_{ij}} \right)^{12} - 18 \left(\frac{\sigma_{ij}}{d_{ij}} \right)^{10} + 4 \left(\frac{\sigma_{ij}}{d_{ij}} \right)^6 \right] + \sum_{(ij) \notin \text{Native}} 4\epsilon_{\text{pd}} \left[\left(\frac{\sigma_{ij}}{d_{ij}} \right)^{12} - \left(\frac{\sigma_{ij}}{d_{ij}} \right)^6 \right]$$

In this case, pairs of beads interacting via native interactions were identified based on the crystal structure of the nucleosome (PDB no. 5NL0). Native interactions were defined between protein beads and ribose or nucleobase beads if any heavy atom of an amino acid falls within 0.5 nm from any heavy atom of that ribose or nucleobase. The ϵ_{ij} for these interactions was set to $2k_B T$ ($\sim 5 \text{ kJ mol}^{-1}$) to ensure these interactions remained formed. For the interactions between the H1 globular domain and the DNA dyad^{88,89}, we reduced the native ϵ_{ij} between protein and DNA to allow for globular domain fluctuations and identified the interaction strength that yielded the best agreement between experimental and computed FRET efficiencies, yielding a value of $1k_B T$ ($\sim 2.5 \text{ kJ mol}^{-1}$). For non-native interactions between the disordered regions of the proteins (histone tails and ProT α) and the DNA, ϵ_{pd} was set to $0.06k_B T$ ($\sim 0.15 \text{ kJ mol}^{-1}$) and σ_{ij} to 0.6 nm . The values of ϵ_{ij} and ϵ_{pd} were chosen to optimize the agreement between simulated and experimentally obtained FRET efficiencies. Note that the optimal strength of non-native interactions, ϵ_{pd} , is the same as that obtained for a non-specific complex between a protein chaperone and DNA hairpin⁸⁶; only the native contact

parameters representing specific interactions needed to be tuned for this system. For simulations with the H1 globular domain rotated by 180° on the nucleosomal dyad, a coordinate transformation was performed and steric clashes relaxed by energy minimization. Native interactions between the rotated globular domain and the DNA were retrieved from the rotationally symmetric list of contacts between the globular domain and the DNA in its native conformation. A summary of all parameter values defining bonded and non-bonded interactions in the models is provided in Supplementary Table 3. In summary, the similarity of the parameters to those used in previous work indicates their transferability. The parameters that were tuned in this work were (1) the DNA base-pairing energy ϵ_{pair} and (2) the strength of the specific, native protein–DNA interactions ϵ_{ij} .

Replica-exchange Langevin dynamics simulations of the nucleosome–H1 complex. Langevin dynamics simulations were performed using a modified version of GROMACS version 5.4.1 (refs. 90,91). The nucleosome was placed at the centre of a box of 30 nm × 40 nm × 30 nm and simulated with and without H1 bound using periodic boundary conditions and charge screening equivalent to 165 mM salt. After energy minimization, 33 replicas were simulated in a temperature range between 298.15 and 648.23 K. Exchange attempts between conformers of neighbouring replicas in temperature space were made every 5 ps and accepted according to the Metropolis criterion. Each replica was run for 1 μs, using a time step of 10 fs and a friction coefficient set at 0.2 ps⁻¹. Particle velocities for each replica were randomly seeded according to a Boltzmann distribution. Interaction energies were calculated in direct space using a cut-off of 2.5 nm, with neighbour searching performed every 0.1 ps.

To test the influence of the FRET dyes on the simulation results, we performed a set of simulations in which the dyes were represented explicitly. Each dye and linker was described by five beads, reflecting the approximate equivalence to a five-amino-acid chain⁹², linked by bonds with a length of 0.38 nm and bond angles of 110° (the dihedral term was omitted). The interaction between the dyes and the protein or DNA was characterized by a weakly attractive short-range interaction energy, with $\epsilon = 0.001 \text{ kJ mol}^{-1}$ and $\sigma = 0.6 \text{ nm}$. The fourth and the fifth beads carried a charge of -1 each to reflect the total charge of -2 of the Alexa fluorophores used in the measurements. Mean FRET efficiencies were calculated from simulations according to the inter-bead distance distributions, $P(r)$, of the fluorescently labelled residues:

$$\langle E \rangle = \int E(r) P(r) dr$$

and the Förster equation:

$$E(r) = \frac{1}{1 + \left(\frac{r}{R_0}\right)^6},$$

using the Förster radius, R_0 , of 5.4 nm of the Alexa Fluor 488/594 dye pair. The agreement between E from experiments and simulations was quantified by the concordance correlation coefficient⁹³, ρ_c , between the two datasets:

$$\rho_c = \frac{2\rho\sigma_{\text{exp}}\sigma_{\text{sim}}}{\sigma_{\text{exp}}^2 + \sigma_{\text{sim}}^2 + (\mu_{\text{exp}} - \mu_{\text{sim}})^2},$$

where σ_{exp} and σ_{sim} indicate the standard deviations, μ_{exp} and μ_{sim} the mean values and ρ the linear (Pearson) correlation coefficient between the values from experiments and simulations, respectively. The concordance correlation coefficient is a stricter measure than the linear correlation coefficient: ρ_c is in general smaller than ρ and is equal to it only if $\sigma_{\text{exp}} = \sigma_{\text{sim}}$ and $\mu_{\text{exp}} = \mu_{\text{sim}}$.

Langevin dynamics simulations of the nucleosome–H1 complex in the presence of ProTα. Langevin dynamics simulations of the nucleosome were performed at a concentration of ProTα of ~10 μM, by placing one molecule of ProTα and the nucleosome bound to H1 in a cubic box of 55 nm × 55 nm × 55 nm. Six independent simulations of the association of ProTα with the H1–nucleosome complex were run at 298.15 K for ~1.4 μs each with the same H1–nucleosome parameters optimized to match the equilibrium FRET data using a modified version of Gromacs 2019 (refs. 90,91), and the same simulation parameters as above. The number of contacts between H1 and either ProTα or the nucleosomal DNA was determined as the number of pairs of beads, one from each molecule, that were within 1.0 nm of each other.

To sample the dissociation of H1 from the nucleosome (with or without ProTα), umbrella sampling was used (implemented using the Plumed plug-in, version 2.5.3 (ref. 94)), with the bias applied to the distance between the centre of mass of the globular domain (residues 23–97) of H1 and the centre of mass of the linker DNA residues contacting the globular domain in the native complex. For distances between 0 and 8 nm, 24 umbrella windows with equally spaced centres and a force constant of 100 kJ mol⁻¹ nm⁻² were used, and from 8 to 32 nm, a further 24 equally spaced windows with a force constant of 10 kJ mol⁻¹ nm⁻² were used, for a total of 48 windows. In addition to the bias applied between H1 and

the nucleosome, a weak harmonic bias with force constant 1 kJ mol⁻¹ nm⁻² was applied between H1 and the centre of mass of any ProTα present to ensure that ProTα was consistently bound in all umbrella windows. Replica exchange moves between adjacent umbrellas were attempted every 500 steps⁹⁵. Potentials of mean force (PMFs) were reconstructed from the equilibrated portion of the trajectories using the weighted histogram analysis method⁹⁶, and the Jacobian contribution $-2k_B T \ln r$ was subtracted. This procedure was performed without ProTα present; with either one or two full-length ProTα molecules; and with the N-terminal (ProTα-N, residues 1–56) and C-terminal (ProTα-C, residues 57–112) halves of ProTα; and PMFs were determined in each case. The dissociation constants K_D were determined by integration of the PMFs via^{64,97}

$$\frac{1}{K_D} = 4\pi N_A \int_0^b \exp[-F(r)/k_B T] r^2 dr,$$

where N_A is Avogadro's number, $F(r)$ is the PMF shifted so that $\lim_{r \rightarrow \infty} F(r) = 0$ and b is the radius defining the maximum extent of the bound state. This approach yielded dissociation constants for H1 from the nucleosome without ProTα, with one ProTα, with two ProTα, with ProTα-N and with ProTα-C, respectively, of $4.1 \times 10^{-17} \text{ M}$, $9.4 \times 10^{-13} \text{ M}$, $1.3 \times 10^{-12} \text{ M}$, $3.3 \times 10^{-17} \text{ M}$ and $5.5 \times 10^{-14} \text{ M}$.

Reporting Summary. Further information on research design is available in the Nature Research Reporting Summary linked to this article.

Data availability

Data supporting the findings of this study are available within the paper and its Supplementary Information. Source data are provided with this paper.

Code availability

A custom WSTP add-on for Mathematica (Wolfram Research) used for the analysis of single-molecule fluorescence data is available upon request and at <https://schuler.bioc.uzh.ch/programs>. A modified version of GROMACS was used for coarse-grained simulations, which is available at <https://github.com/bestlab/gromacs-2019.4.git>.

References

- Scott, K. A., Steward, A., Fowler, S. B. & Clarke, J. Titin; a multidomain protein that behaves as the sum of its parts. *J. Mol. Biol.* **315**, 819–829 (2002).
- Kilic, S., Bachmann, A. L., Bryan, L. C. & Fierz, B. Multivalency governs HP1α association dynamics with the silent chromatin state. *Nat. Commun.* **6**, 7313 (2015).
- Lowary, P. T. & Widom, J. New DNA sequence rules for high affinity binding to histone octamer and sequence-directed nucleosome positioning. *J. Mol. Biol.* **276**, 19–42 (1998).
- Dyer, P. N. et al. Reconstitution of Nucleosome core particles from recombinant histones and DNA. *Methods Enzymol.* **375**, 23–44 (2004).
- Müller, B. K., Zaychikov, E., Bräuchle, C. & Lamb, D. C. Pulsed interleaved excitation. *Biophys. J.* **89**, 3508–3522 (2005).
- Klehs, K. et al. Increasing the brightness of cyanine fluorophores for single-molecule and superresolution imaging. *ChemPhysChem* **15**, 637–641 (2014).
- Aitken, C. E., Marshall, R. A. & Puglisi, J. D. An oxygen scavenging system for improvement of dye stability in single-molecule fluorescence experiments. *Biophys. J.* **94**, 1826–1835 (2008).
- Ha, T. & Tinnefeld, P. Photophysics of fluorescence probes for single-molecule biophysics and super-resolution imaging. *Ann. Rev. Phys. Chem.* **63**, 595–617 (2012).
- Schuler, B. Application of single molecule Förster resonance energy transfer to protein folding. *Methods Mol. Biol.* **350**, 115–138 (2007).
- Nettels, D., Gopich, I. V., Hoffmann, A. & Schuler, B. Ultrafast dynamics of protein collapse from single-molecule photon statistics. *Proc. Natl Acad. Sci. USA* **104**, 2655–2660 (2007).
- Gopich, I. V., Nettels, D., Schuler, B. & Szabo, A. Protein dynamics from single-molecule fluorescence intensity correlation functions. *J. Chem. Phys.* **131**, 095102 (2009).
- Holmstrom, E. D. et al. Accurate transfer efficiencies, distance distributions, and ensembles of unfolded and intrinsically disordered proteins from single-molecule FRET. *Methods Enzymol.* **611**, 287–325 (2018).
- Zheng, W. et al. Inferring properties of disordered chains from FRET transfer efficiencies. *J. Chem. Phys.* **148**, 123329 (2018).
- Gopich, I. V. & Szabo, A. Theory of the energy transfer efficiency and fluorescence lifetime distribution in single-molecule FRET. *Proc. Natl Acad. Sci. USA* **109**, 7747–7752 (2012).
- Sisamakris, E., Valeri, A., Kalinin, S., Rothwell, P. J. & Seidel, C. A. M. Accurate single-molecule FRET studies using multiparameter fluorescence detection. *Methods Enzymol.* **475**, 455–514 (2010).
- Hellenkamp, B. et al. Precision and accuracy of single-molecule FRET measurements—a multi-laboratory benchmark study. *Nat. Methods* **15**, 669–676 (2018).

82. Zosel, F., Mercadante, D., Nettels, D. & Schuler, B. A proline switch explains kinetic heterogeneity in a coupled folding and binding reaction. *Nat. Commun.* **9**, 3332 (2018).
83. Chung, H. S. et al. Extracting rate coefficients from single-molecule photon trajectories and FRET efficiency histograms for a fast-folding protein. *J. Phys. Chem. A* **115**, 3642–3656 (2011).
84. Viterbi, A. J. Error bounds for convolutional codes and an asymptotically optimum decoding algorithm. *IEEE Trans. Inf. Theory* **13**, 260–269 (1967).
85. Karanicolas, J. & Brooks, C. L. III The origins of asymmetry in the folding transition states of protein L and protein G. *Protein Sci.* **11**, 2351–2361 (2002).
86. Kim, Y. C. & Hummer, G. Coarse-grained models for simulations of multiprotein complexes: application to ubiquitin binding. *J. Mol. Biol.* **375**, 1416–1433 (2008).
87. Yakovchuk, P., Protozanova, E. & Frank-Kamenetskii, M. D. Base-stacking and base-pairing contributions into thermal stability of the DNA double helix. *Nucleic Acids Res.* **34**, 564–574 (2006).
88. Zhou, B. R. et al. Structural insights into the histone H1–nucleosome complex. *Proc. Natl Acad. Sci. USA* **110**, 19390–19395 (2013).
89. Zhou, Y. B., Gerchman, S. E., Ramakrishnan, V., Travers, A. & Muyldermans, S. Position and orientation of the globular domain of linker histone H5 on the nucleosome. *Nature* **395**, 402–405 (1998).
90. Berendsen, H. J. C., van der Spoel, D. & van Drunen, R. GROMACS: a message-passing parallel molecular dynamics implementation. *Comp. Phys. Comm.* **91**, 43–56 (1995).
91. van der Spoel, D. et al. GROMACS: fast, flexible, and free. *J. Comput. Chem.* **26**, 1701–1718 (2005).
92. Aznauryan, M. et al. Comprehensive structural and dynamical view of an unfolded protein from the combination of single-molecule FRET, NMR, and SAXS. *Proc. Natl Acad. Sci. USA* **113**, E5389–E5398 (2016).
93. Lin, L. I. A concordance correlation coefficient to evaluate reproducibility. *Biometrics* **45**, 255–268 (1989).
94. Tribello, G. A., Bonomi, M., Branduardi, D., Camilloni, C. & Bussi, G. Plumed 2: new feathers for an old bird. *Comput. Phys. Commun.* **185**, 604–613 (2014).
95. Sugita, Y., Kitao, A. & Okamoto, Y. Multidimensional replica-exchange method for free-energy calculations. *J. Chem. Phys.* **113**, 6042–6051 (2000).
96. Kumar, S., Rosenberg, J. M., Bouzida, D., Swendsen, R. H. & Kollman, P. A. The weighted histogram analysis method for free-energy calculations on biomolecules. I. The method. *J. Comp. Chem.* **13**, 1011–1021 (1992).
97. Shoup, D. & Szabo, A. Role of diffusion in ligand binding to macromolecules and cell-bound receptors. *Biophys. J.* **40**, 33–39 (1982).

Acknowledgements

We thank I. König for providing ProTα, K. Buholzer and F. Sturzenegger for helpful discussion, F. Büchler and N. Wyss for excellent technical assistance and the Functional Genomics Center Zurich for performing mass spectrometry. This work utilized the computational resources of the National Institutes of Health HPC Biowulf cluster (<http://hpc.nih.gov>) and of Piz Daint at the CSCS Swiss National Supercomputing Centre. This project was funded by the Novo Nordisk Foundation (P.O.H.), the Carlsberg Foundation (P.O.H.), The Boehringer Ingelheim Fonds (S.K.), the Swiss National Science Foundation (B.S. and B.F.), École Polytechnique Fédérale de Lausanne (B.F.) and the Intramural Research Program of the National Institute of Diabetes and Digestive and Kidney Diseases at the National Institutes of Health (R.B.B.).

Author contributions

P.O.H., D.M., R.B.B. and B.S. designed the research; P.O.H. and S.K. prepared the reconstituted nucleosomes; P.O.H., M.B.B., A.B., A.S., S.K. and B.F. prepared the fluorescently labelled and/or unlabelled proteins; P.O.H. and A.S. performed the single-molecule experiments; P.O.H., A.S., D.N. and B.S. analysed the single-molecule data; D.M. and R.B.B. performed and analysed the simulations; R.B.B., B.F. and B.S. supervised the research; and P.O.H. and B.S. wrote the paper with help from all authors.

Competing interests

The authors declare no competing interests.

Additional information

Supplementary information The online version contains supplementary material available at <https://doi.org/10.1038/s41557-021-00839-3>.

Correspondence and requests for materials should be addressed to Pétur O. Heidarsson, Robert B. Best or Benjamin Schuler.

Peer review information *Nature Chemistry* thanks the anonymous reviewers for their contribution to the peer review of this work.

Reprints and permissions information is available at www.nature.com/reprints.

Reporting Summary

Nature Research wishes to improve the reproducibility of the work that we publish. This form provides structure for consistency and transparency in reporting. For further information on Nature Research policies, see our [Editorial Policies](#) and the [Editorial Policy Checklist](#).

Statistics

For all statistical analyses, confirm that the following items are present in the figure legend, table legend, main text, or Methods section.

n/a Confirmed

- The exact sample size (n) for each experimental group/condition, given as a discrete number and unit of measurement
- A statement on whether measurements were taken from distinct samples or whether the same sample was measured repeatedly
- The statistical test(s) used AND whether they are one- or two-sided
Only common tests should be described solely by name; describe more complex techniques in the Methods section.
- A description of all covariates tested
- A description of any assumptions or corrections, such as tests of normality and adjustment for multiple comparisons
- A full description of the statistical parameters including central tendency (e.g. means) or other basic estimates (e.g. regression coefficient) AND variation (e.g. standard deviation) or associated estimates of uncertainty (e.g. confidence intervals)
- For null hypothesis testing, the test statistic (e.g. F , t , r) with confidence intervals, effect sizes, degrees of freedom and P value noted
Give P values as exact values whenever suitable.
- For Bayesian analysis, information on the choice of priors and Markov chain Monte Carlo settings
- For hierarchical and complex designs, identification of the appropriate level for tests and full reporting of outcomes
- Estimates of effect sizes (e.g. Cohen's d , Pearson's r), indicating how they were calculated

Our web collection on [statistics for biologists](#) contains articles on many of the points above.

Software and code

Policy information about [availability of computer code](#)

Data collection SymPhoTime 64 (PicoQuant) was used for single-molecule data collection. A modified version of GROMACS was used for coarse-grained simulations, which is available at <https://github.com/bestlab/gromacs-2019.4.git>.

Data analysis A custom WSTP add-on for Mathematica (Wolfram Research, v.11, v.12) was used for the analysis of single-molecule fluorescence data and is available upon request and at <https://schuler.bioc.uzh.ch/programs>.

For manuscripts utilizing custom algorithms or software that are central to the research but not yet described in published literature, software must be made available to editors and reviewers. We strongly encourage code deposition in a community repository (e.g. GitHub). See the Nature Research [guidelines for submitting code & software](#) for further information.

Data

Policy information about [availability of data](#)

All manuscripts must include a [data availability statement](#). This statement should provide the following information, where applicable:

- Accession codes, unique identifiers, or web links for publicly available datasets
- A list of figures that have associated raw data
- A description of any restrictions on data availability

All data supporting the findings of this study are available within the paper and its Supplementary Information. The raw data are available from the corresponding authors upon reasonable request.

Field-specific reporting

Please select the one below that is the best fit for your research. If you are not sure, read the appropriate sections before making your selection.

Life sciences Behavioural & social sciences Ecological, evolutionary & environmental sciences

For a reference copy of the document with all sections, see [nature.com/documents/nr-reporting-summary-flat.pdf](https://www.nature.com/documents/nr-reporting-summary-flat.pdf)

Life sciences study design

All studies must disclose on these points even when the disclosure is negative.

Sample size	Single-molecule experiments on freely diffusing molecules involved 1000-15000 molecules, and experiments involving surface-immobilized molecules included 10-50 molecules for every experimental condition. The sample size was found to satisfactorily describe the conformational distribution and kinetics in the ensemble. Binding and unbinding rates were computed from a minimum (although usually many more) of 100 events each. The length of the simulations was at least 100 times the typical distance correlation time within bound or unbound states, corresponding to a minimum of 100 independent samples within each state.
Data exclusions	Freely diffusing bursts arising from molecules with only a single fluorophore and with < 50 photons were excluded from analysis. Surface immobilized time traces were inspected to ensure that no substantial brightness variations were occurring (e.g., drift of the molecule's position, long-lived dark states, nucleosomal unwrapping events, or background fluctuations). Single-step photobleaching indicated that only one molecule was present in the confocal volume. For the simulations, the first half of each trajectory was discarded as equilibration.
Replication	All main results were successfully reproduced using different samples (protein, DNA, or nucleosome preparations), and measured on different days in fresh buffers.
Randomization	Samples were not randomized.
Blinding	Experiments were not blinded.

Reporting for specific materials, systems and methods

We require information from authors about some types of materials, experimental systems and methods used in many studies. Here, indicate whether each material, system or method listed is relevant to your study. If you are not sure if a list item applies to your research, read the appropriate section before selecting a response.

Materials & experimental systems

n/a	Involvement in the study
<input checked="" type="checkbox"/>	<input type="checkbox"/> Antibodies
<input checked="" type="checkbox"/>	<input type="checkbox"/> Eukaryotic cell lines
<input checked="" type="checkbox"/>	<input type="checkbox"/> Palaeontology and archaeology
<input checked="" type="checkbox"/>	<input type="checkbox"/> Animals and other organisms
<input checked="" type="checkbox"/>	<input type="checkbox"/> Human research participants
<input checked="" type="checkbox"/>	<input type="checkbox"/> Clinical data
<input checked="" type="checkbox"/>	<input type="checkbox"/> Dual use research of concern

Methods

n/a	Involvement in the study
<input checked="" type="checkbox"/>	<input type="checkbox"/> ChIP-seq
<input checked="" type="checkbox"/>	<input type="checkbox"/> Flow cytometry
<input checked="" type="checkbox"/>	<input type="checkbox"/> MRI-based neuroimaging